Università di Pisa

SCIENZE MATEMATICHE FISICHE E NATURALI
Corso di Laurea Magistrale in Fisica della Materia

Tesi di laurea magistrale:

A programmable metrological standard based on the quantum Hall effect

Candidato:
Luigi Caputo

Relatore:
Prof. Stefano Roddaro

Relatore esterno:
Dr. Stefan Heun

Anno Accademico 2019-2020
Appello di maggio 2021

A programmable metrological standard based on the quantum Hall effect
Luigi Caputo, May 2021

Contents

Introduction

The Quantum Hall Effect (QHE) is the quantum limit of the Hall effect and its main manifestation is the quantization of the Hall coefficient in high-mobility two-dimensional electron systems, when subjected to low temperature conditions and to a strong perpendicular magnetic field. This effect emerges from the quantization of the cyclotron electron orbits into "Landau levels". The effect was discovered by Klaus von Klitzing while working on a high purity silicon-based MOSFET, and he observed this phenomenon in the MOSFET's inversion layer at liquid helium temperature and in a 15 T magnetic field [1]. Quantized Hall conductance has found extremely useful metrological applications, since it occurs at integer multiples of e^2/h, where e is the electron charge and h is Plank's constant, i.e. it is a combination of two fundamental constants. Experimentally, resistance measurements yield this value with an astonishing precision (up to 12 decimal figures [2]). Starting from the so-called metrological triangle, which involves the use of other quantum mechanical effects such as the Josephson effect and single electron transport, it was considered whether it is possible to obtain the values of h and e with metrological precision [3].

The importance of the resistance quantum value $R_K = h/e^2$ is not just connected to the fundamental constants but interesting as a resistance standard for electrical calibration. The quantum Hall resistance is equal to $R_H = R_K/\nu$, where the integer ν is called filling factor, which corresponds to the number of filled Landau levels. Ideally, one would like to have different filling factors on the same sample to achieve, in a single chip, different standards to calibrate resistances of different orders of magnitude. Many approaches have been proposed to achieve this goal. In particular: (i) cryogenic current comparators (CCC), which allow current (and thus resistance) rescaling with metrological precision; (ii) so called QHARSs (Quantum Hall Array of Resistance Standards), which consist of a network of Hall bars yielding a rational fraction q/p of the resistance R_K. Both these methods are affected by limitations. The networks used in QHARS rely on Ohmic contacts between individual Hall bars that introduce measurement errors due to stray voltages, parasitic resistances or other non-local effects [4]. Differently, CCCs typically require an additional cryogenic system, and they can be affected by noise when trying to compare resistance values $\ll R_K$. Finally, both these methods yield a fixed resistance standard and to obtain a different value one has to use a different QHARS or a CCC with a different number of windings. This thesis is based on a recently-proposed QH circuit architecture [5] that, thanks to a precise and tunable voltage bisection

scheme, can yield any four-wire resistance of the form $R = \frac{k}{2^n}\frac{R_K}{2}$. The integer n indicates the number of bisection stages whose configurations set the value $1 \leq k \leq 2^n$. While the basic working principle of this QH circuit has been experimentally demonstrated, its ultimate precision is still unknown.

This thesis has two targets: (*i*) to experimentally quantify the maximum bias voltage compatible with the QH effect, since this directly affects the top achievable precision; (*ii*) to study the influence of a finite output resistance of the QH circuit as this again affects the precision of the resistance standards produced by the circuit. The thesis is organized as follows:

- Chapter 1. Theory
  The basic theory behind the QHE and how a 2D electron gas can be realized in a semiconductor heterostructure is illustrated.

- Chapter 2. Quantum Hall metrology
  The concept of a metrological standard will be illustrated along with the most common techniques to compare resistance values and to achieve different fractional values of R_K using a single Hall bar or an array of Hall bars. The working of an edge mixer will be illustrated, that is the fundamental building block of the actual device, which is the topic of this thesis.

- Chapter 3. Device fabrication
  In this section we report step by step the fabrication of a Hall bar device that includes the edge mixers that have been characterized in this thesis. The actual device has also been fabricated on the same chip, even though not used for the measurements.

- Chapter 4. Experimental apparatus
  The experimental work of this thesis has been carried out at Laboratorio NEST of Scuola Normale Superiore in Pisa. The magneto-transport data were obtained making use of a ^{3}He cryostat to achieve 300 mK temperature. The basic working principle of the cryostat will be illustrated, along with the instrumentation and the wiring of the sample.

- Chapter 5. Experimental results
  In this section, the characterization of the Hall-bar device will be described: we characterized the two dimensional electron gas, IV curves of the edge mixers have been checked, and the Hall bar operating at $\nu = 2$ and $\nu = 4$, yielding different fractions of R_K, has been explored.

- Chapter 6. Output resistance
  The influence of a finite output resistance on the QH circuit will be discussed, both with a numerical and an analytical approach. This contributes to an understanding of the precision achievable with this kind of devices.

1

Theory

This chapter is devoted to summarize physical concepts useful later on: transport, the (integer quantum) Hall effect, and two-dimensional electron gases (2DEGs).

1.1 2DEGs in heterostructures

For our purpouse, a GaAs/AlGaAs heterojunction is illustrated in Fig. 1, that is formed upon contact of undoped GaAs and n-doped AlGaAs. When in contact,

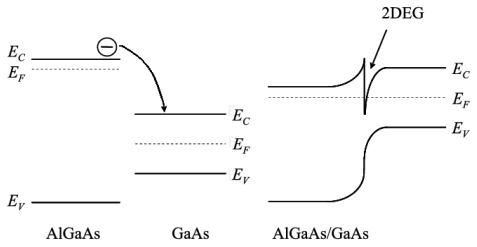

Figure 1: GaAs/AlGaAs heterojunction

the Fermi energies of the two materials align to equilibrate the carrier densities, but the bands bend to mantain ΔE_c and ΔE_v (the difference in conduction and valence band energy in the two materials) constant at the junction, following the Anderson rule [6].

From Fig. 1 we see that a 2D electron gas (2DEG) is formed at the junction, where the electrons are confined in the growth direction of the heterostructure

by the band potential and are free to move on the junction plane.

1.2 The Hall effect

It is useful to make a brief recap of the classical Hall effect. Fig. 2 is taken as a reference, where the square represents a 2D metallic slab.

In general, we have:

$$\vec{J} = \sigma \vec{E}, \tag{1.1}$$

where $\vec{J}$ is the current density, $\vec{E}$ is the electric field given by $(V/L, 0, 0)$, and σ the conductivity tensor. In the case $B = 0$, the conductivity is diagonal for isotropic materials and $V_H = 0$, and the conductance is in general $\rho = \sigma^{-1}$. In the case $\vec{B} = B\hat{z}$, σ is a non diagonal tensor, because we have build-up of opposite charges on the sides of the sample, so that a potential drop $V_H = E_y W$ along W will develop.

$$\vec{J} = (J_x, J_y) \tag{1.2}$$

$$\vec{E} = (E_x, E_y) \tag{1.3}$$

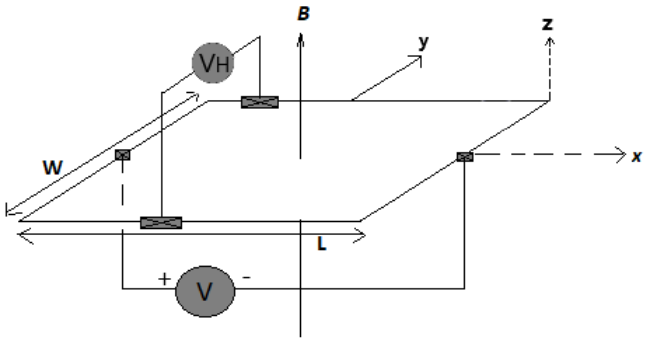

Figure 2: Hall slab with reference frame. V is a voltage generator, V_H is a voltmeter.

The 2D conductivity has the form:

$$\sigma = \begin{pmatrix} \sigma_{xx} & \sigma_{xy} \\ \sigma_{yx} & \sigma_{yy} \end{pmatrix}. \tag{1.4}$$

Now we want to find ρ_{xx}, ρ_{xy} and the associated Hall resistance R_H. To do it, we solve the equation of motion for one electron in steady state using the

Drude theory:

$$\dot{\vec{p}} = -e(\vec{E} + \vec{v} \times \vec{B}) - \frac{\vec{p}}{\tau}, \tag{1.5}$$

where τ is the electron relaxation time. At steady state we have $\dot{\vec{p}} = 0$ and

$$\vec{v} = -\frac{e\tau}{m^*}(\vec{E} + \vec{v} \times \vec{B}), \tag{1.6}$$

where $\mu_e = -e\tau/m^*$ is the mobility. By definition $\vec{J} = n(-e)\vec{v}$ and so we can write

$$\vec{J} = \frac{ne^2\tau}{m^*}(\vec{E} - \frac{\vec{J}}{ne} \times \vec{B}) \tag{1.7}$$

And so:

$$\vec{E} = \frac{m^*}{ne^2\tau}\vec{J} + \vec{J} \times \frac{\vec{B}}{ne}. \tag{1.8}$$

Since $\vec{B} = B\hat{z}$ and considering $\vec{E}$ and $\vec{J}$ components we get:

$$\vec{E} = \rho\vec{J} = \begin{pmatrix} \frac{m^*}{ne\tau} & \frac{B}{ne} \\ -\frac{B}{ne} & \frac{m^*}{ne\tau} \end{pmatrix} \vec{J}. \tag{1.9}$$

Note that $\rho_{xx} = \rho_{yy}$ (isotropy) and $\rho_{xy} = -\rho_{yx}$ (sign of V_H). From Eq. (1.9):

$$\rho_{xy} = \frac{B}{en} \tag{1.10}$$

$$\rho_{xx} = \frac{m^*}{\tau e^2 n} \tag{1.11}$$

$$R_H \equiv \frac{\rho_{yx}}{B} = -\frac{1}{en}. \tag{1.12}$$

In case we have a semiconductor, this approach is valid as long as we assume a single band and type of carriers present [6], and the mass m has been replaced by the effective band mass m^*.

1.3 Landau levels of a 2DEG

Now the quantum mechanical problem of an electron in a two dimensional electron gas in an external magnetic field is treated. This two dimensional electron gas is formed at the junction of our GaAs/AlGaAs heterostructure.

We write the Hamiltonian minimally coupled with a magnetic field $\vec{B} = (0, 0, B)$ represented by the vector potential $\vec{A} = (-yB, 0, 0)$ in the Landau

gauge.

$$H = \frac{(p_x - \frac{e}{c}yB)^2}{2m} + \frac{p_y^2}{2m} \tag{1.13}$$

Since the problem is translationally invariant along x, we can look for solution of the form $\psi = e^{ikx}\phi(y)$. Expanding the terms we can rewrite Eq. (1.13) in the form of Eq. (1.14).

$$H = \frac{p_y^2}{2m} + \frac{1}{2}m\omega_c^2(y - y_0)^2, \tag{1.14}$$

where $y_0 = \frac{\hbar k_x}{eB}$, $\omega_c = \frac{eB}{m}$ is the cyclotron frequency, and $l = \sqrt{\frac{\hbar}{eB}}$ the magnetic length. The Hamiltonian in Eq. (1.14) is the same as a harmonic oscillator, then its eigenvalues are:

$$E_{nk_x} = \left(n + \frac{1}{2}\right)\hbar\omega_c. \tag{1.15}$$

From the form of the Hamiltonian in Eq. (1.14), we can see that the electrons move freely along x and they oscillate inside a strip of magnetic length l along y, thus in the wave equation $\psi = e^{ikx}\phi(y)$, $\phi(y)$ is the 1D harmonic oscillator eigenvalue and so we can say that $p_x = \hbar k_x$. It is important to remind to substitute the mass m with the effective band mass $m^* = 0.067m_e$ of an electron in a 2DEG of a GaAs/AlGaAs heterostructure. In a 2DEG, electrons are confined along z and free in the xy plane.

Let us now calculate the 2D density of states in the case B $= 0$ ($DOS(E, 0)$) and B $\neq 0$ ($DOS(E, B)$).

$$DOS(E) = \sum_k \delta(E(k) - E) \approx \int \delta(E(k) - E)\frac{Sd^2k}{(2\pi)^2} \tag{1.16}$$

$$DOS(E, 0) = \int \delta(\frac{\hbar^2k_x^2 + \hbar^2k_y^2}{2m} - E)\frac{Sd^2k}{(2\pi)^2} = \frac{S}{2\pi}\frac{m}{\hbar^2} \tag{1.17}$$

The $DOS(E, 0)$ is then constant in energy. When B $\neq 0$, we no longer have a dispersion in k, so we have atomic-like levels, and the number of states previously between those levels are "squashed" inside the discrete levels making them degenerate. As shown in Fig. 3, we have then a DOS that is a series of delta functions with $\sum_n N_L\delta(E - E_{nk_x})$, where N_L is the degeneracy of the Landau levels.

N_L is given by the maximum extension of the harmonic oscillator, i.e. $y_0 = W$ from which we find k_x^{max} and the k_x is quantized in units of $2\pi/L$ for periodic

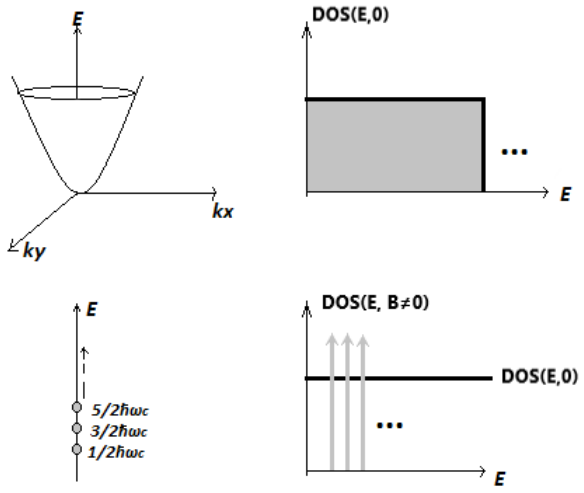

Figure 3: Levels and DOS in absence and presence of a magnetic field.

boundary conditions along x, then:

$$N_L = k_x^{max} \frac{L}{2\pi} = \frac{eBS}{h} = \frac{\phi(B)}{\phi_0} = D_0 \hbar \omega_c, \tag{1.18}$$

where N_L is also the maximum number of states going inside one of the states in $D_0 = DOS(E, 0)$, $\phi(B)$ is the magnetic flux $B \cdot S$ and $\phi_0 = hc/e$ is the elementary flux quantum. The states are the ones between two discrete levels i.e. in the energy interval $\Delta E = \hbar\omega_c$ and that is equal to $D_0 \hbar \omega_c$.

The number of filled Landau levels is given by:

$$\nu = \frac{N}{N_L} = \frac{N}{\frac{\phi(B)}{\phi_0}} = \frac{n\hbar}{eB}. \tag{1.19}$$

The part of ν exceeding its integer part is the filling fraction of the last partially populated Landau level.

1.4 The quantum Hall effect

In this section the quantum Hall effect is illustrated, in particular the integer quantum Hall effect that is of relevance for our purpose.

According to Eq. (1.12) and Eq. (1.19) we can write:

$$\rho_{xy} = \frac{ehB}{nche^2} = \frac{1}{\nu}\frac{h}{e^2}, \tag{1.20}$$

where ν is an integer. We will explain the physical meaning of Eq. (1.20), according to the results of the previous section. The quantization into Landau levels also affects ρ_{xx}: now $\rho_{xx} = \rho_{xx}(B)$. Fig. 4 shows the profiles of the two resistivities vs B, and the blue steps are described by Eq. (1.20).

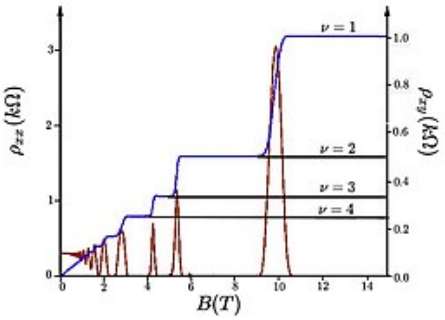

Figure 4: Integer Quantum Hall Effect.

Reminding that $N_L \propto B$, so varying B, the occupation of the Landau levels also changes, and consequently E_F changes. Now, let us consider a defect-free finite sample. If E_F falls between the Landau levels, this means that all the levels with $E < E_F$ are fully occupied and so the conduction of electrons cannot occur in the bulk of the sample because there is an energy gap and the bands shown in Fig. 5 are flat and no hole-electron excitation can occur at low T. If E_F happens to be equal to one of these Landau levels, the conduction can occur in the bulk of the sample, since the Landau level E_F will not be fully occupied, and we will have a spike in ρ_{xx}. Since the sample is of finite size, we have for the electrons a confining potential at the edges (Fig. 5) that can cross E_F if E_F falls between Landau levels: in this manner the conduction only occurs at the edge of the sample.

Because all the conduction electrons freely flow on the edge with the same chemical potential (here Fermi energy for simplicity sake), the longitudinal potential drop is zero and so $\rho_{xx} = 0$. These oscillations in ρ_{xx} are called Shubnikov-de Haas (SdH) oscillations (red curve in Fig. 4).

With a finite slab, just its edges introduce a defect and actually thanks to defects we can measure the plateaus in ρ_{xy} when E_F lies between levels. Fig. 6 shows that the introduction of defects modifies the density of states so that it

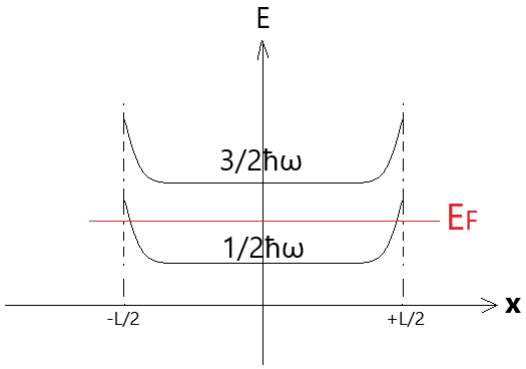

Figure 5: Energy levels of a finite defect-free sample, along x.

is finite between levels and the deltas are broadened and the degeneracy lifted. ρ_{xy} depends only on ν and so it stays the same for E_F between levels, to then going to another value when E_F crosses a Landau level. The steps seen in ρ_{xy} are now sharper and wider. The dependence of ν with E_F is shown in Fig. 7.

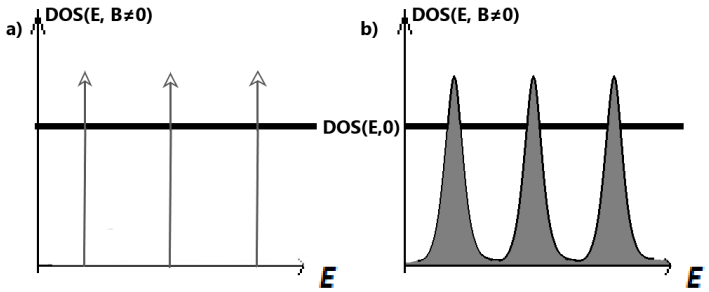

Figure 6: a) Density of states in absence of defects, b) density of states in presence of defects.

If there are bulk impurities, thus producing a local potential that can intersect E_F, currents can flow around defects forming the so-called localized states. These states are current loops that do not interfere with electron transport from one end of the sample to the other.

In the classical picture visible in Fig. 8 the electron orbits near the edges cannot fully close and so the electrons bounce and the net effect is current at edges of the material, the number of current edges is given by the filling factor ν.

If we also include the electron spin interaction with the magnetic field, each Landau level splits into two, separated by $B\mu_B$, where μ_B is the Bohr magneton,

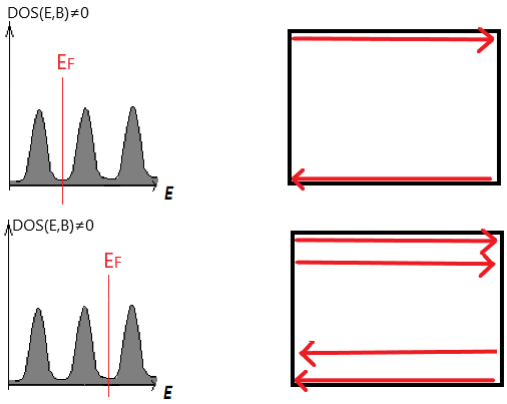

Figure 7: Edge currents with varying E_F (between $\nu = 1$ and $\nu = 2$) in a finite sample.

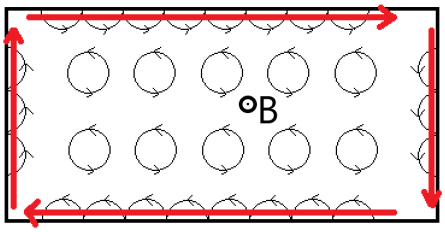

Figure 8: Edge states due to the finite size of the sample (skipping orbits).

like Fig. 9 that shows the Zeeman of the first Landau level. Right moving currents travel on the upper edge and left moving on lower edge, as in Fig. 8. At equilibrium $V = 0$ the currents cancel.

Considering $T \ll \hbar\omega_c$ (which is close to our temperature range for the experiment) and a finite V, we can find the resistance of one current edge.

$$\mu_R - \mu_L = (-e)V \tag{1.21}$$

$$I = (-e)\int_{k_L}^{k_R} v_x(k)\frac{dk}{2\pi} = \frac{e^2}{2\pi\hbar}\int_{\mu_L}^{\mu_R} dE(k) = \frac{e^2}{h}V \tag{1.22}$$

$$R_{1edge} = \frac{V}{I} = \frac{h}{e^2} = R_K \tag{1.23}$$

The number of Landau levels intersected by the chemical potential μ_R for right moving channels and μ_L for left moving channels, gives the filling factor ν and the number of current edges, so in general $I = \nu\frac{e^2}{h}V$ and so $R_H = R_K/\nu$ where

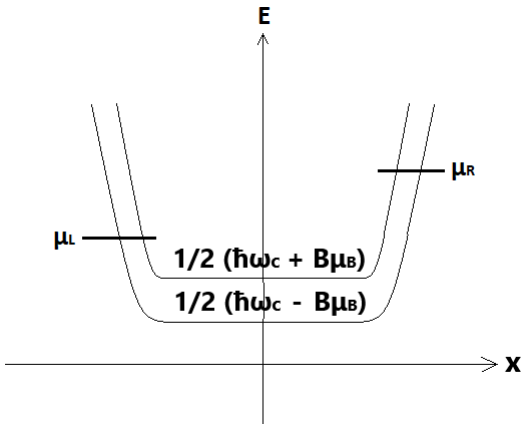

Figure 9: Out of equilibrium (V $= \mu_R - \mu_L \neq 0$) levels of the finite sample ($\nu = 2$) with a confining potential (finiteness of the sample) and filled up to the chemical potentials.

$R_K \approx 25.8\,\mathrm{k}\Omega$ is the von Klitzing constant. In general $R_H = \frac{R_K}{\nu}$ regardless of the form of the confining potential. What is important is how many Landau levels the chemical potential intersects.

The states at the border of the sample are chiral ($v_x = \frac{\partial E(k)}{\hbar k}$ has opposite sign on the two edges) and do not mix in the bulk if W is sufficiently wide (generally $W \gg l$). Real samples also contain bulk impurities that develop current edges too, so there must be as few as possible to avoid mixing edges and maintain chirality (in our Drude picture $\tau\omega_c \gg 1$, so high magnetic fields and low temperatures help).

For $B \to 0$ we recover the classical value for ρ_{xx} and ρ_{xy}.

1.5 Metal-semiconductor contacts

In metrological measurements, contacts are a critical issue. The resistance standard must not be affected by the contact resistance and then they must be reliable and resilient to thermal cycles between room temperature and cryogenic temperatures. In general it is possible to classify two types of metal-semiconductor contacts: As in Fig. 10, Ohmic contacts and Schottky contacts. The first type has Ohmic $I - V$ characteristics and is achieved when the semiconductor conduction band bends to form a thin barrier at the junction with the metal. We need this contact to measure voltages and current flow in our 2DEG device, as electrons can easlity tunnel the barrier. Schottky contacts are achieved when a wider barrier is formed and are useful to obtain a potential

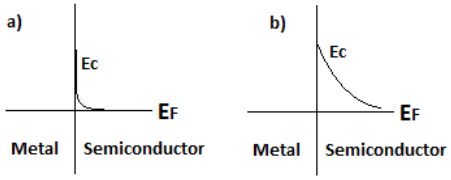

Figure 10: a) Ohmic contact, b) Schottky contact.

barrier and block the electron flow through the contact.

In our case field effect is achieved by creating a gating structure composed superficially by this last type of contact plus a first layer of a dielectric insulator. The gating is used to modify E_F at equilibrium or the electron density in our 2DEG so we can control the filling factor ν in chosen regions of the sample (Fig.11). Ohmic contacts are achieved via annealing of the metal deposited on

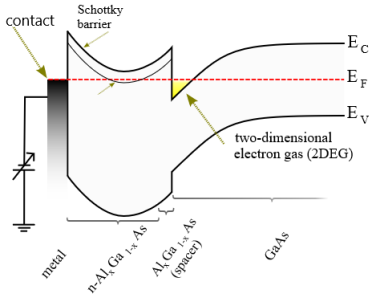

Figure 11: Example of a Schottky contact on a hetero-junction.

the heterostructure, which strongly n-dopes the junction with the layers of the hetero-structure and thins the Schottky barrier (see chapter 3). An illustration of the contacts is in Fig. 12.

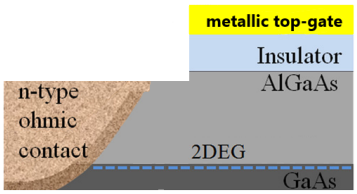

Figure 12: Device contacts.

Such contacts can have a resistivity as low as $\rho_c \sim 10^{-6}\,\Omega \times \mathrm{cm}^2$ [7, 8]. The best alloy that do not deteriorate over time was found to be AuGeNi.

2

Quantum Hall metrology

This chapter is devoted to expose the methods used to compare a metrological resistance standard to other resistances. Common metrological standards will be discussed, along with their drawbacks compared to the novel device illustrated in the thesis.

2.1 The potentiometric method

The easiest way to compare a generic resistance with a Hall resistance is through the potentiometric method. We now describe what is shown in Fig. 13.

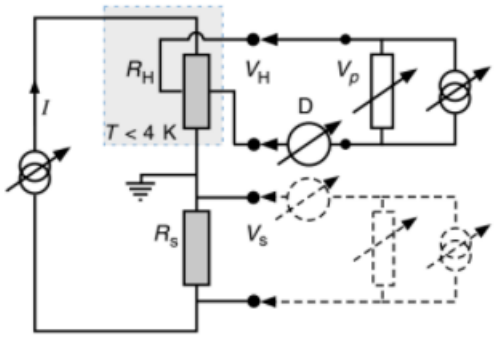

Figure 13: Potentiometric method [2]

An Hall bar is put in series with a resistance R_s to be compared, and a current is injected with a DC current (I) generator. One of the two transversal terminals to measure R_H on the Hall bar, a high impedence voltage detector

in series with R_H is attached. The circuit with R_H is closed with another DC current (I) generator in parallel with a potentiometer R_P that sets the voltage V_P across this other current generator. With the usage of the high impedance detector, R_P is set so that $V_P = V_H$, and so $D = 0$ (balance condition). Now the circuit including the detector and the generator in parallel with R_P, is moved across the resistance R_S and the detector measures $V_S - V_P = V_S - V_H = (R_S - R_K)I$, if this quantity is zero then $R_S = R_K$, otherwise the detector is not balanced.

Multiple measurements are performed, for example changing the sign of I, in order to lower the uncertainty due to the instability of the current generators.

2.2 Current comparators

Instead of comparing voltages we can compare currents.

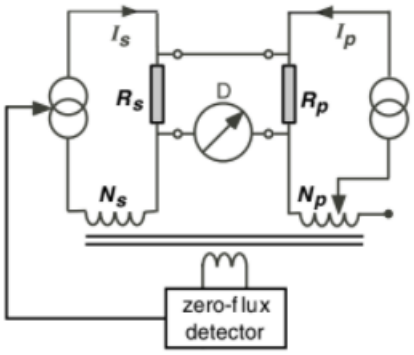

Figure 14: Current comparator. Zero flux is achieved when $N_S I_S = N_P I_P$ [2]

As in Fig. 14, a feedback system adjusts the current through R_S and an inductance in series, so to achieve a zero flux condition $N_S I_S = N_P I_P$ through a magnetometer mutually coupled with this inductance and another inductance in series with R_P in a separated circuit. Adjusting the winding number of this last inductance so that the same voltage is applied across R_S and R_P (the detector shown in Fig. 14 is balanced) we have $I_S R_S = I_P R_P$. Thus $R_P/R_S = N_P/N_S$, so it is possible to quantify generic resistances with one another.

The accuracy of this method can be improved by using a SQUID as a magnetometer, as shown in Fig. 15, realizing a so-called cryogenic current comparator or CCC for short.

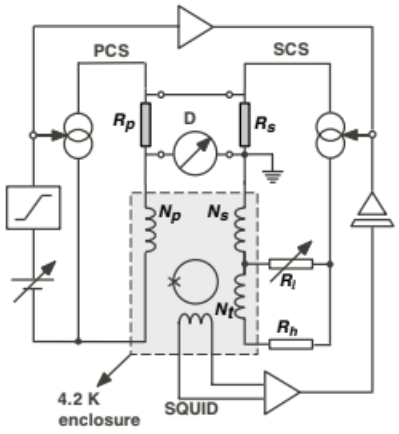

Figure 15: Cryogenic current comparator that uses a potentiometer to achieve the detector balance [2].

2.3 QHARS

When two resistances to be compared are very different from each other (for example 100 Ω and $R_K \approx 25.8\,\mathrm{k\Omega}$), the methods illustrated lose precision because more significant digits need to be taken into account when measuring R_P/R_S, or the electrical noise becomes more prominent. We then would like a reliable resistance standard customizable in order of magnitude.

More conventional metrological standards of this kind are the so called QHARS. These devices consist in a series of Hall bars with equal filling factor. The connection between them determine for the terminals injecting a known current I, a potential difference that gives R = q'R_K, where q' is the coefficient of effective resistance (CER) that depends on the wiring topology and is a rational fraction. For example, like in Fig. 16, to obtain a resistance value of the form $R = R_K/2^n$ you can imagine putting 2^n Hall bars at $\nu = 2$ in series with each other, and all in parallel with the current generator I. The connections in QHARS introduce stray resistances, but by increasing the number of connections between pairs of bars they overall vanish according to Eq. 2.1 [9, 10], where α is the number of connections between two Hall bars and $\epsilon < 1$ is a weight factor accounting for the significance of the correction to R_{tot} due to these stray resistances.

$$R_{tot} = R + \epsilon^{\alpha} R_{stray} \tag{2.1}$$

It is also possible to short edge contacts on a single Hall bar to then measure R with two voltage probes as shown in Fig.17 [11]. It was seen by solving the

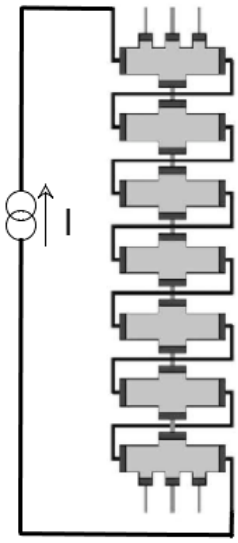

Figure 16: Example of a QHARS. Voltage drops across different gray floating contacts yields different fractions of R_K (4-wire resistance).

node equations (next section will provide details) that $R = \frac{q}{p} R_k$ is obtained and was determined that $2n$ connections give a $q = 1...n$ and a $p = 1...n$.

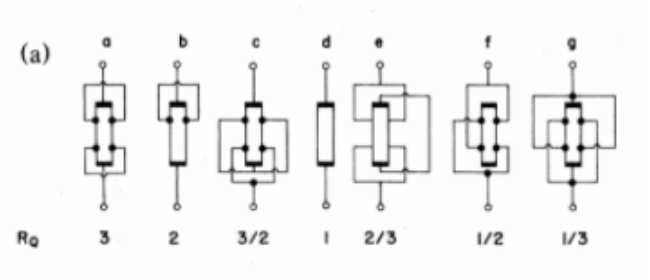

Figure 17: Single hall bars with various shorts on their edge contacts. R_Q is a fraction of R_K.

2.4 A novel device architecture

This section explains the working of the novel metrological device [5]. To do this we first illustrate the effect on the edge potential drops for a Hall bar with

different ν on the bulk, achieved with a gating system. We show that we can obtain various fractions of R_K, that we explicitly calculate and that will be useful for comparison with the measurements. Finally we illustrate the novel metrological device called bisector.

2.4.1 Single edge mixer

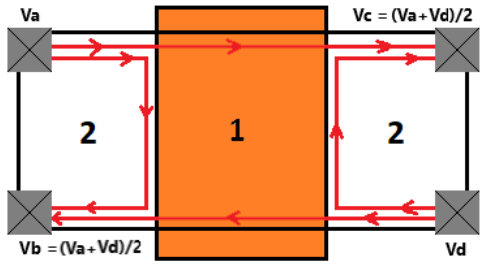

Figure 18: One Hall barrier (clockwise chirality).

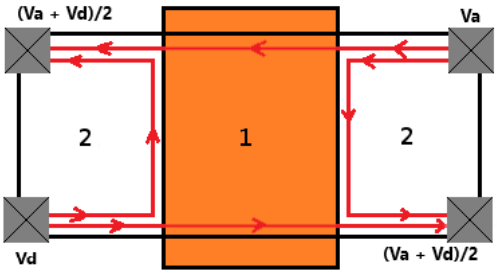

Figure 19: One Hall barrier (anticlockwise chirality).

The fundamental element of our device consists in two regions with $\nu = 2$ separated by a $\nu = 1$ region or "barrier" that can be switched to $\nu = 2$ with a gating system. When the barrier is in the $\nu = 1$ state, this element acts like a voltage bisector, since the barrier reflects one edge channel as, illustrated in Fig. 18 and Fig. 19.

We discuss now voltage drop values that we expect along and across the single barrier according to the Landauer-Büttiker theory [12], i.e. from a contact at voltage V originates an edge current with each edge carrying a current $I = V/R_K$. The voltage drops for this kind of devices can be then calculated by writing the current conservation equation at each contact. Using Fig. 19 as a reference (bar at $\nu = 2$) and setting $V_a = 0$ so to bias the bar with V_d voltage,

we expect to measure along the bar and across the barrier a voltage drop $V_d/2$, the same value is found along the barrier. V_d value is found on one diagonal of the bar and on the other diagonal we have a zero voltage drop. If we have $\nu = 2$ under the barrier, we find a zero voltage drop along the bar, V_d on both diagonals and along the barrier. If we have $\nu = 0$ (pinch-off) under the barrier, we find V_d voltage drop along the bar and on both diagonals, along the barrier we find a zero voltage drop. The sign of the voltage drops depend on the order of the voltage probes.

In this way we have achieved a bisection scheme that allows to measure the fraction $V_d/2I = R_K/2$ across the barrier.

2.4.2 Double edge mixer

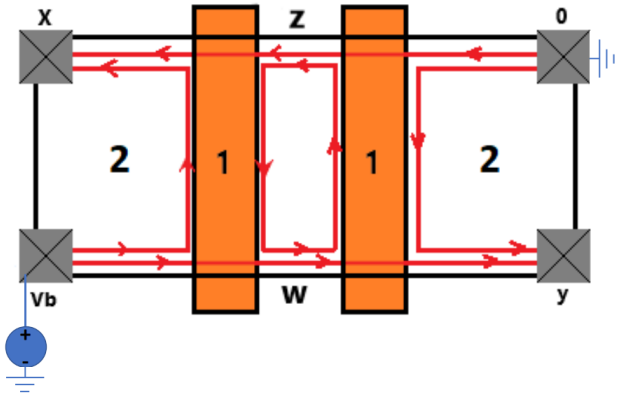

Figure 20: Two barriers at $\nu = 1$ with counter clock-wise chirality. The bar is biased with voltage V_b.

Now we study the case with two barriers at $\nu = 1$ as in Fig. 20. We can calculate the voltage we expect to find on the diagonal and on the two bottom contacts across the two barriers, by solving the following system of equations that comes from solving the node equations for the currents entering or leaving each contact:

$$\begin{cases} x = \frac{V_b}{2} + \frac{z}{2} \\ y = z = \frac{w}{2}. \end{cases} .$$

From these equations we find: $y - x = -\frac{V_b}{3}$ and $V_b - y = \frac{2V_b}{3}$, respectively the \ diagonal voltage drop and the longitudinal voltage drop. For both barriers in pinch-off or at $\nu = 2$ we have the same value we would measure on a single barrier.

By adding another barrier we have increased the number of fractions of R_K we can achieve.

2.4.3 Results for the double barrier ($\nu = 4$)

For the Hall bar at $\nu = 4$, we have a larger plethora of voltage drop values, all of them can be calculated as in the previous section. We report here two tables, one for bottom longitudinal voltage drop and for the \ diagonal that will be useful for the thesis later. Left and right gate refers to Fig. 20.

Left gate ν \ Right gate ν	1	2	3	4
1	6/7	4/5	10/13	3/4
2	4/5	2/3	4/7	1/2
3	10/13	4/7	2/5	1/4
4	3/4	1/2	1/4	0

Table 1: Bottom longitudinal voltage drop in unit of V_b.

Left gate ν \ Right gate ν	1	2	3	4
1	-5/7	-3/5	-7/13	-1/2
2	-3/5	-1/3	-1/7	0
3	-7/13	-1/7	1/5	1/2
4	-1/2	0	1/2	1

Table 2: \ Diagonal voltage values in voltage bias unit.

2.4.4 Bisector

It is useful to illustrate the equivalence of the single barrier scheme in Fig. 21(a-b) to the scheme shown in Fig. 21(c-d). We assume to be working at field values giving $\nu = 2$. In fact if one writes down the node equations for this alternative configuration and solves for V_{TL}, V_{TR}, V_{BL} and V_{BR}, the same relations as the single barrier will be found:

$$\begin{cases} V_{E5} = V_{E6} = (V_{TL} + V_{E4})/2 \\ V_{E4} = V_{TR} = (V_{E6} + V_{E2})/2 \\ V_{BL} = V_{E3} = (V_{E5} + V_{E1})/2 \\ V_{E1} = V_{E2} = (V_{E3} + V_{BR})/2 \end{cases}.$$

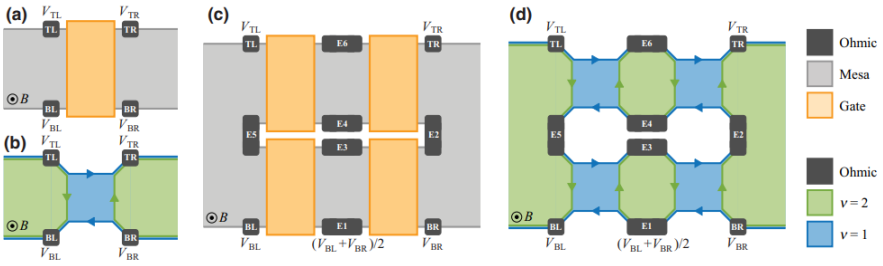

Figure 21: Useful equivalence.

.

Now we have all the ingredients to describe the whole device. If we take Fig. 21(c) and change the topography of the barriers like in Fig. 22, in particular we move one of the two lower barriers on the side, we obtain a stackable element (stage) with upper side contacts $V_{R,n}$ and $V_{L,n}$ and so at the bottom side contacts $V_{R,n+1} = (V_{R,n} + V_{L,n})/2$ and $V_{L,n+1} = V_{L,n}$ or $V_{R,n+1} = (V_{R,n} + V_{L,n})/2$ and $V_{L,n+1} = V_{L,n}$ depending on which barrier is moved upward. Contacts on the same edge and not separated by a barrier can be fused together. Following this logic we can fabricate two gates in the position of both configurations: these two gates are switchable to $\nu = 2$ or $\nu = 1$ with an applied potential, so we obtain multiple configurations on a single device. Right barrier at $\nu = 1$ and left barrier at $\nu = 2$ correspond to configuration 1 and the opposite to configuration 0, we will call other combinations "non-standard". Stacking n stages, $2n$ standard configurations are possible, we will now study the value of $V_{L,n+1}$ and $V_{R,n+1}$ as a function of the lateral barriers configuration. Defining $\Delta V_n = V_{R,n} - V_{L,n}$ we can rewrite for configuration 1 of the n-th stage:

$$V_{L,n+1} = V_{L,n} + \frac{\Delta V_n}{2} \tag{2.2}$$

$$V_{R,n+1} = V_{R,n} \tag{2.3}$$

For configuration 0:

$$V_{R,n+1} = V_{R,n} - \frac{\Delta V_n}{2} \tag{2.4}$$

$$V_{L,n+1} = V_{L,n}. \tag{2.5}$$

For both configurations $\Delta V_{n+1} = \Delta V_n/2$. If we introduce the binary digit c_{n+1}

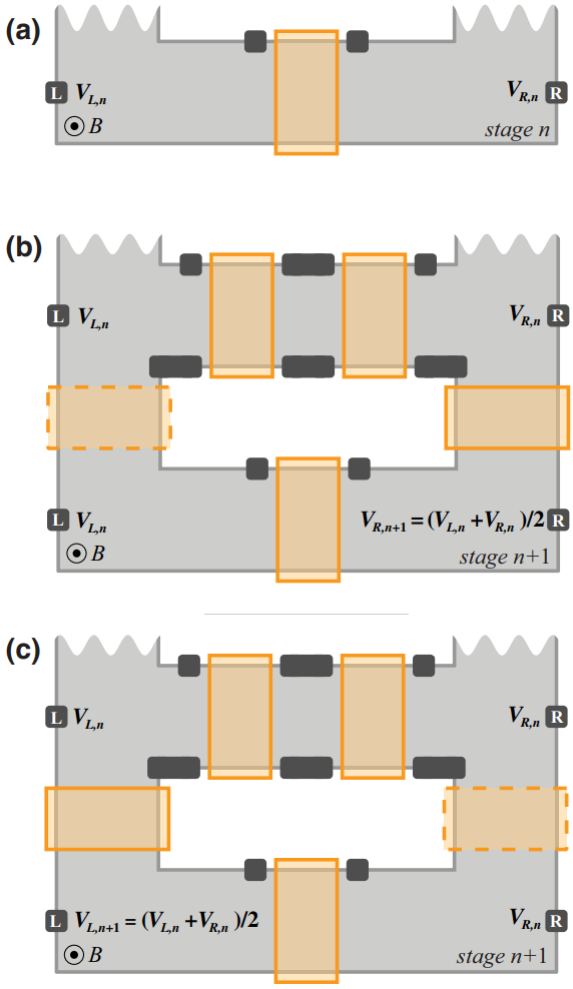

Figure 22: Topography change of a single barrier.

to indicate the configuration of the $(n+1)$-th stage:

$$V_{L,n+1} = V_{L,n} + c_{n+1}\Delta V_{n+1} \tag{2.6}$$

$$V_{R,n+1} = V_{L,n+1} + \Delta V_{n+1}. \tag{2.7}$$

If we iteratively apply Eq. (2.6) and Eq. (2.7) to the initial stage with upper

contacts $V_{L,0}$ and $V_{R,0}$:

$$V_{L,n} = V_{L,0} + \sum_{i=1}^{n} c_i \frac{\Delta V_0}{2^i} = V_{L,0} + \sum_{i=1}^{n} c_i 2^{n-i} \frac{\Delta V_0}{2^n} = V_{L,0} + (k-1)\frac{\Delta V_0}{2^n} \quad (2.8)$$

$$V_{R,n} = V_{L,0} + k\frac{\Delta V_0}{2^n}, \quad (2.9)$$

where k is the decimal representation of the binary digits c_i and runs from 1 to 2^n. If we inject a current I through V_{R0} and V_{L0} setting $V_{R0} = 0$, using the Landauer-Büttiker formalism [12], we find $\Delta V_0 = I\frac{R_K}{2}$ and thus:

$$\frac{\tilde{V}}{I} = \frac{V_{R,n} - V_{L,0}}{I} = \frac{R_K}{2}\frac{k}{2^n}. \quad (2.10)$$

We have then obtained a reprogrammable resistance value $R = \frac{R_K}{2}\frac{k}{2^n}$ for metrological purposes that can be measured with a four-probe technique as shown in Fig. 23.

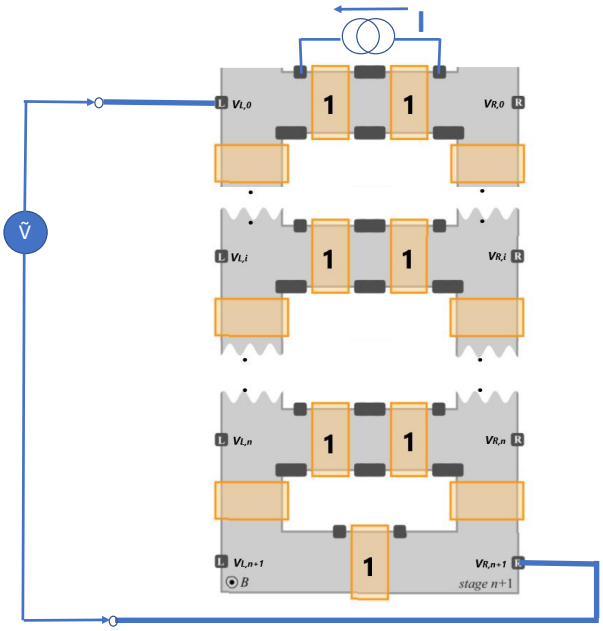

Figure 23: Stacked stages and four-probe measurement.

It must be said that the mixing of the edge channels, operated by the gates of a real device, may create channels with different chemical potentials, but these

last ones are equilibrated by the presence of intermediate Ohmic contacts [13, 14] between adjancent barriers.

The advantage of our novel device consists in the fact that its elements scale linearly with n and no internal Ohmic contacts are needed, so they do not contribute to perturb the output resistance standard (in the last chapter we will discuss what it does and how) and the customizable values are more numerous compared to a QHARs with the same number of elements.

3

Device fabrication

This chapter explains the fabrication of the novel metrological device [5].

The device chip is a GaAs/AlGaAs heterostructure grown at the Weizmann institute. We have at our disposal 1/4 of wafer with the specifics given in Table 3. The range of values for the doping ('n') in Tab.3 refers to a carrier

n	$(3.0 \div 3.9) \times 10^{11}\,\mathrm{cm}^{-2}$
μ	$(7.2 \times 10^{3} \div 5.0 \times 10^{6})\,\mathrm{cm}^2/\mathrm{Vs}$
2DEG depth	670 Å

Table 3: Some fabrication parameters.

density measurement at $T = 300\,\mathrm{K}$ (lower value) and at $T = 4\,\mathrm{K}$ (higher value), furthermore 'n' increases with the presence of ambient light and decreases in its absence (persistent photoconductivity). The same goes for the mobility μ.

The wafer is cut with a diamond tip and applying pressure on the opposite side of the cut, a chip is made by making it slide along one of the crystalline planes. The wafer portions used are illustrated in Fig. 24.

3.1 Ohmic contacts fabrication

Before proceeding with the actual device contact fabrication, we fabricated a series of Ohmic contacts on the test chip in Fig. 24. Each of the contacts undergoes a current annealing procedure with various current values (11.0, 11.5 and 12.0 A), the best current value was found to be 11.5 A. At a temperature of $T = 2.5\,\mathrm{K}$, we measure the contact resistances and it turns out that they are negligible with respect to the $100\,\Omega$ line resistance of the cryostat.

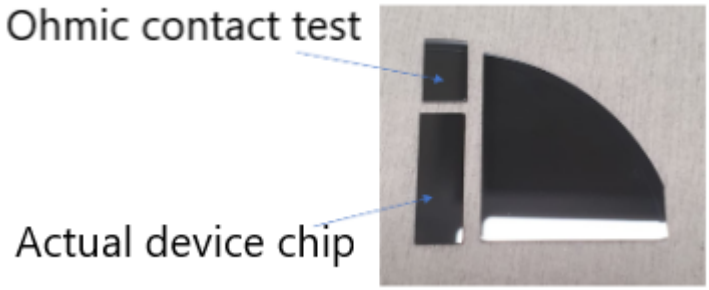

Figure 24: Wafer.

Then we proceed with the fabrication of the actual device. Two chips are made, each contains 4 nominally identical copies of a 4 stage bisector and two Hall bars with gate electrodes (or edge mixers). The Hall bar devices permit to study the behaviour of two individual beam splitters (gates) and to verify the basic transport properties of the heterostructure, that, after all the fabrication process, could result degraded.

We start by cleaning the obtained chips via the following procedure:

1. 50 °C Acetone for 5 mins
2. Isopropanol for 30 seconds
3. Drying with inert gas N_2

The first two steps use polar solvents and are useful to remove organic and non-organic impurities. Acetone tends to leave residues after evaporation (e.g. its oligomers), so isopropanol is used as an additional washing agent. The choice of the solvents has been dictated by their relative non-toxicity to other compounds used for the same purpose. The inert gas clearly prevents the formation of unwanted oxides.

From now on we continue with the Ohmic contact lithography. The following is the procedure used:

1. Prebaking at 120 °C for 60 seconds
2. Application of S1813 positive resist with 4000 rpm spinner for 60 seconds
3. Baking at 90 °C for 60 seconds (removal of the resist solvent)
4. Laserwriter exposure with dose 90 mJ/cm^2 and objective x5 (2 μm resolution)

5. Bath in MF319 developer for 60 seconds (from data sheet)
6. Washing in deionized water (DIW)
7. Drying with N_2

Prebaking is needed to get rid of possible humidity residues. The resist thickness can be found from Fig. 25 (from the resist datasheet) and from this it is possible to determine the energy dose of the laserwriter (Fig. 26) $\sim 90\,\mathrm{mJ/cm^2}$ (values for a 436 nm wavelength). The contact pattern to transfer on the resist is shown in Fig. 27. A pre-etching is performed so that the resist-free zones of the

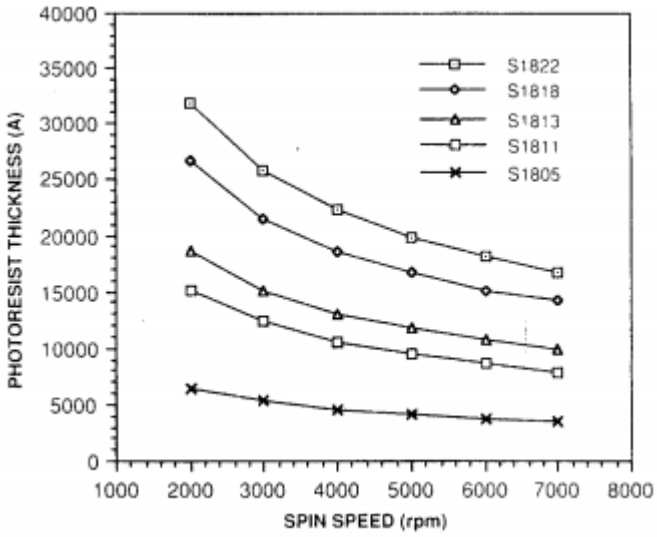

Figure 25: Spinner speed vs resist thickness. For 4000 rpm, we read about 1.4 μm of thickness.

semiconductor are engraved a bit. In this way the metallic contact will diffuse better inside the semiconductor during the annealing process.

1. Etching with H_3PO:H_2O_2:H_2O (3:1:40) for 30 (chip 1) and 60 (chip 2) seconds (etch rate is about 100 nm/min).
2. Washing in DIW
3. Drying with N_2

The metal used is a NiAuGe multilayer and is deposited with a thermal evaporator from Sistec (Fig. 28). We proceed according to the following scheme:

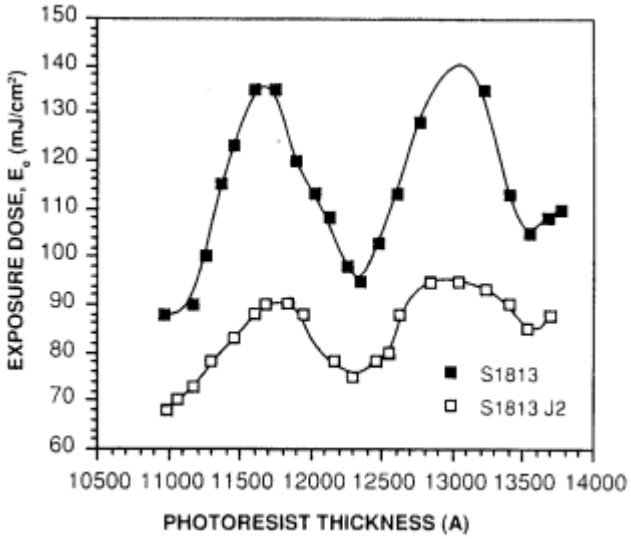

Figure 26: Energy flux to completely expose the resist. The wave-like profile is due to the fact that for a certain thickness stationary waves are formed inside the resist and in this way the radiation is trapped inside the resist for longer times [15].

1. Chamber evacuation, down to $P < 10^{-5}$ mbar.
2. Ni evaporation. 10 nm thickness, rate 1 Å/sec.
3. Eutectic AuGe 88:12 evaporation. 200 nm thickness, rate $2 - 3$ Å/sec.
4. Ni evaporation. 10 nm thickness, rate 1 Å/sec.
5. Au evaporation. 100 nm thickness, rate 2 Å/sec.
6. Hot acetone (50 °C) based lift-off for 10 min (cyclically repeated process untill all the excess metal is completely removed).
7. Drying with N_2.

When the lift-off is difficult to perform (for example when the metal thickness is as big as in this case), it is possible to make use of an ultrasound bath or a syringe.

Now we can proceed with the current annealing. The annealing process makes so that, increasing the metal temperature, it diffuses inside the semiconductor and via segregation Germanium partially substitutes Gallium. The former has one more electron in its outer shell than the latter, effectively strongly

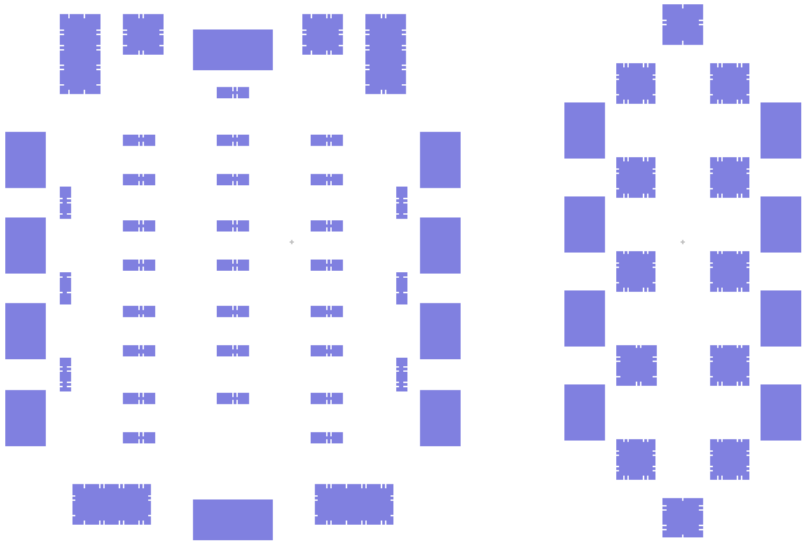

Figure 27: Ohmic contact pattern.

doping the semiconductor underneath; this phenomenon occurs in a 350 °C-450 °C temperature window. The result is a metal-n^{++} junction, that is effectively an Ohmic contact due to the extremely thin Schottky barrier, through which electrons can easily tunnel.

1. Power supply calibration at 11.5 Å.
2. Sample mounting.
3. Evacuating the chamber via a membrane pump.
4. Flux of N_2 at 0.5 l/min.
5. Annealing with 11.5 Å for 60 seconds.
6. Vent with N_2.

The choice of the annealing current was made based on the earlier tests done on the tests contacts, given the fact that the current-temperature conversion is not reliable because it strongly depends on the materials upon which the annealing is performed (according to previous calibrations here it should correspond to 450 °C).

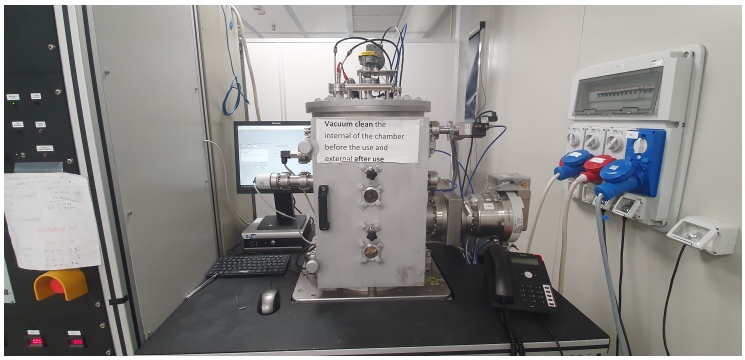

Figure 28: Evaporator with vacuum chamber.

3.2 Mesa fabrication

In an similar fashion to the contact lithography, the mesa lithography is performed with pattern in Fig. 29. The mesa is the region of the chip that contains the 2DEG that is etched away in other parts. The Hall current will flow on its boundary.

1. Prebake at 120 °C for 60 seconds to remove humidity.
2. S1805 spinning at 4000 rpm for 60 seconds
3. Bake at 90 °C for 60 seconds
4. Laserwriter with dose 90 mJ/cm^2 and objective x5 (2 μm resolution)
5. MF319 developer 60 seconds
6. Stop (generous) in deionazed water (DIW)
7. Drying with N_2

Then the etching process:

1. Etching with H_3PO:H_2O_2:H_2O (3:1:40) for and 60 seconds.
2. Drying in DIW.
3. Drying in N_2.

The Ohmic contacts are fabricated before the mesa because the mesa etching can contaminate the surface and thus affect contact fabrication process.

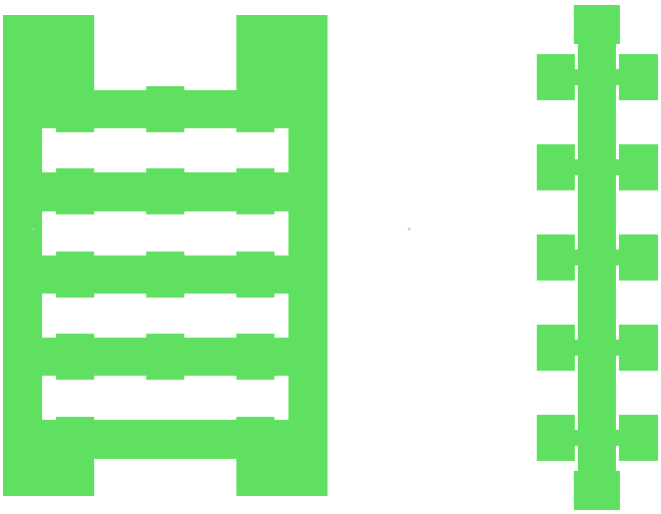

Figure 29: Mesa pattern.

3.3 Gates fabrication

Finally we proceed to make the gate electrodes with pattern shown in Fig. 30, in this case they will be Schottky contacts (so no annealing is performed). In this case a different recipe is used because we need a resist underetch, so that we can have a good lift-off.

The process described is needed to harden the uppermost part of the resist, so that the inferior part will be removed much easier during the development process, creating in this way an underetching.

1. Prebake at 120 °C for 60 sec to remove humidity.
2. S1805 spinning at 4000 rpm for 60 seconds.
3. Bake at 90 °C for 60 seconds.
4. Predevelopment in MF319 for 120 seconds.
5. Bake at 120 °C for 120 seconds.
6. Laserwriter with dose 90 mJ/cm^2 and x5 objective (2 μm resolution).
7. Development in MF319 for 4 minutes.
8. Stop (generous) in DIW.
9. Drying with N_2.

Figure 30: Gates pattern.

The evaporation has been made with a different kind of evaporator from Kurt-Lesker, simply because aluminium metal is not nominally present as a source for the Sistec evap.

1. Pumping out air up to $P < 10^{-5}$ mbar.
2. Al evap. 50 nm thickness, rate 2 Å/sec.
3. Lift-off with hot acetone (50 °C) for 10 minutes.
4. Isopropanol for 30 seconds.
5. Drying with N_2.

Using aluminium induces less disorder in the electronic system with respect to other alternatives such as Ti/Au [16]. It should be noted that to make a gold gate we also need to employ some kind of bonding material (e.g. titanium, other alternatives includes Cr and Ni but here are of no use, since they are magnetic) because gold would not stick very well. Instead aluminium is typically quite self-adhesive already. It is interesting to note that Al transitions to its superconducting state at a temperature of 1 K and superconductors are known to be poor heat conductors, so one might have efficiency problems in the cool down of the sample. The problem is solved by applying an external critical magnetic field; for Al this is $\sim 0.01T$, the device will operate for field values well above this.

The complete pattern is shown in Fig. 31.

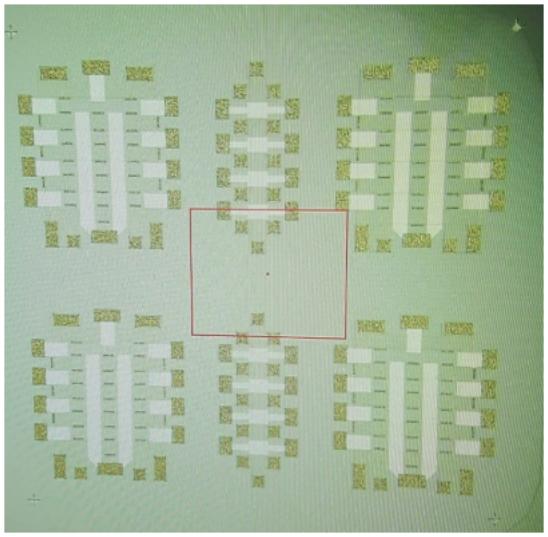

Figure 31: The complete pattern.

3.4 Packaging and wire bonding

The chip is mounted on a 16 dual-in-line chipcarrier shown in Fig. 32, compatible with the cryogenic setups available at NEST. The sample is glued to

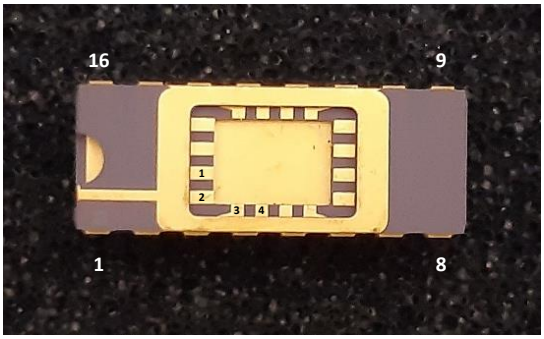

Figure 32: Hall bar chip carrier.

the chipcarrier die with some PMMA. Thermally speaking this is not ideal, but these samples cool down mostly via the bonding wires, so it does not matter so much.

We then bond the gold wires to the chip contacts and to the chip carrier contacts (Fig. 33). From Fig. 34 is possible to see what the bonder tip looks

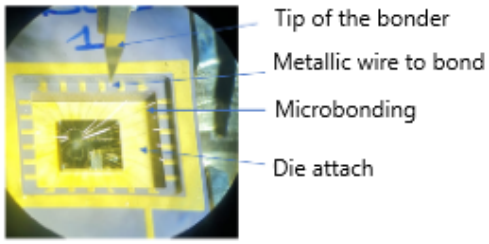

Figure 33: Photo from the bonder microscope.

like: this kind of bonder is called wedge bonder. We have a hole through which the gold wire is held in place and pressed onto the surface. The machine uses ultrasound vibration on the tip simultaneously applying a certain pressure so the gold is made more malleable. Also a hot plate, on which the sample is placed, is used. All the parameters relevant to this process are empirical and substrate dependent. During this process the wire is held in place by a clamp on the back of the tip. Then we perform the other bond by releasing the clamp and positioning the tip over the second contact. With the gold wire still pressed and bonded against the contact and the clamp still clenched, the tip is quickly moved away from the contact: in this way the wire breaks at the bonding point.

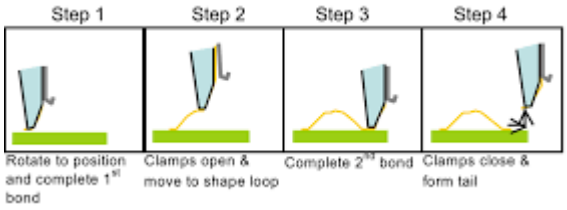

Figure 34: Bonder tip

The final result is shown in Fig. 35.

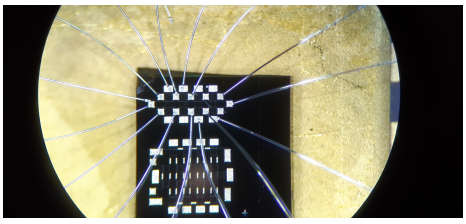

Figure 35: Bonded Hall bar device inside the chip carrier.

4

Experimental apparatus

In this chapter we make an overview of the instrumentation used in the measurements. The latter were performed at the magneto-transport lab in NEST. The device is placed inside a ^{3}He cryostat that can reach temperatures between 250 mK and 300 mK. Then the instrumentation to perform voltage and current measurements is attached to the contacts coming from the cryostat lines connected to the sample contacts.

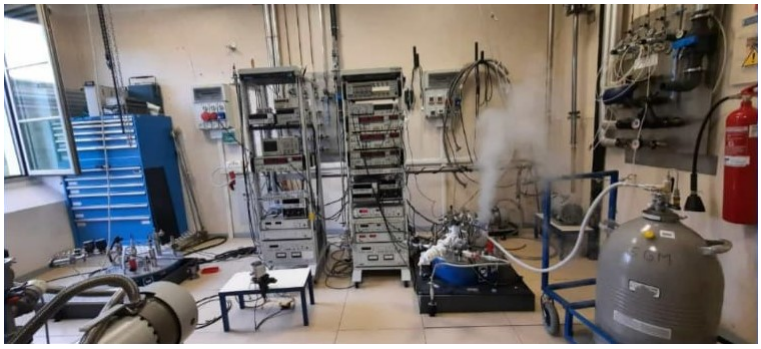

Figure 36: Magneto-transport lab in NEST. N_2 refilling process is visible.

4.1 The cryostat

The cryostat used in the experiment is a Heliox from Oxford Instruments and as said before it is a ^{3}He cryostat. This kind of apparatus is composed of two parts, the insert system and the dewar, and actually works with three gases: ^{3}He, ^{4}He and N_2. The dewar is a tank composed of two intercalated shells. The

inner one contains liquid ^4He gas at a temperature of 4.2 K and can be refilled from an external filling part (helium transfer process, shown in Fig. 37). This part is enclosed by a jacket with a 10^{-6} mbar vacuum. The outer one is a liquid-N_2-refillable shell that further insulates the inner portions from the blackbody radiation of the environment. The N_2 tank is also surrounded by jacket with a 10^{-6} mbar vacuum too. The N_2 is loaded in the tank via another filling part on top of the dewar. These filling parts are not sealed, otherwise the whole setup would explode from the pressure buildup. The internal liquid ^{4}He that evaporates is partially recovered with a pipeline that goes to a condenser that liquifies the gas again in another tank which is used for the helium transfer once the cryostat dewar is almost empty, while the inexpensive N_2 is simply lost.

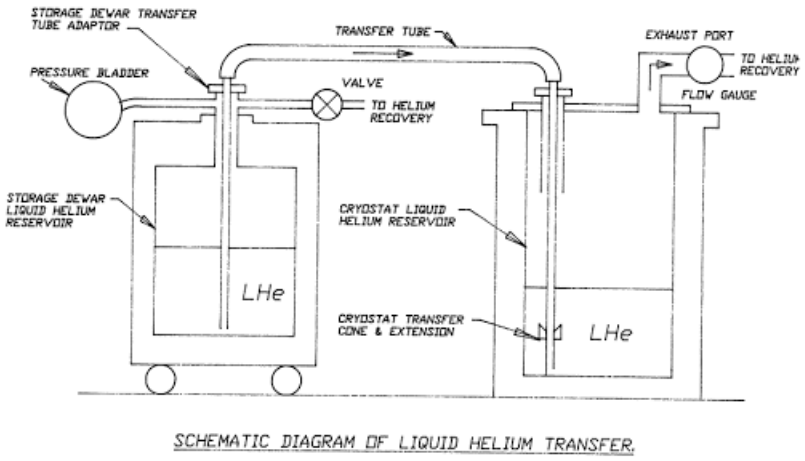

Figure 37: Helium transfer process.

The cryostat dewar is placed in a pit under the floor and is loaded from the top with the insert system. At the bottom of this system there is a sample holder, visible in Fig. 38, from where connection wires from the sample contacts depart. These lines are filtered (see appendix A for details).

The sample is in thermal contact with an upper section that is the hollow sealed stick shown in Fig. 39, kept at low pressure (about 10^{-6} mbar). On the outer side of the stick, at a certain height, there is another hollow section in thermal contact with the inner stick, this section is called 1K pot (see Fig. 42), the reason for this name will be clear in a while. Once the sample is attached, a lid is put on it that tightly seals (Fig. 40), so that vacuum can be performed in the insert system: before bringing down the insert system inside the tank

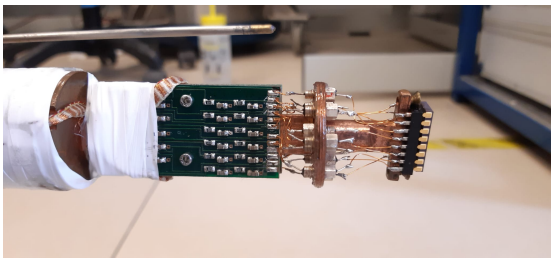

Figure 38: Insert system sample holder. The printed board before the white teflon tape are the filters.

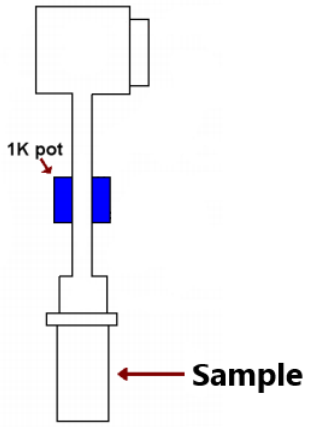

Figure 39: Insert system sketch.

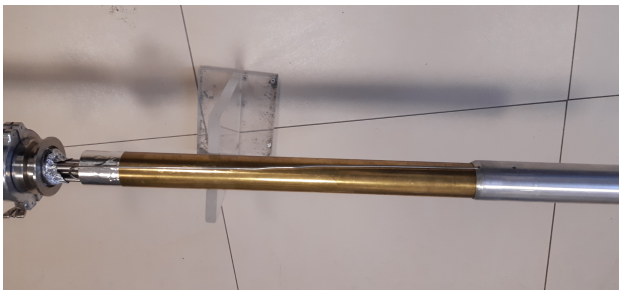

Figure 40: Bottom part of the insert system, covered.

we perform a 10^{-6} mbar vacuum using a turbomolecular pump as in Fig. 41. Then we fill it with some ^{4}He gas: this will act as a heat exchange gas. ^{4}He is continuously fluxed through the 1 K pot section with a small tube connected to the lab piping system, so to prevent the formation of ice from water vapour.

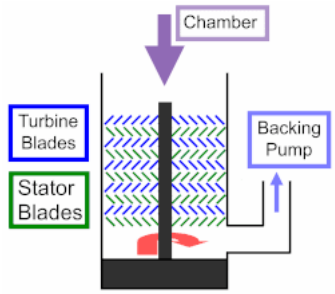

Figure 41: A turbo pump works with rotor blades forcing gas molecules to move in a certain direction (towards a scroll pump for example).

Now the whole setup is ready to be inserted inside the dewar tank.

4.1.1 Cooldown procedure

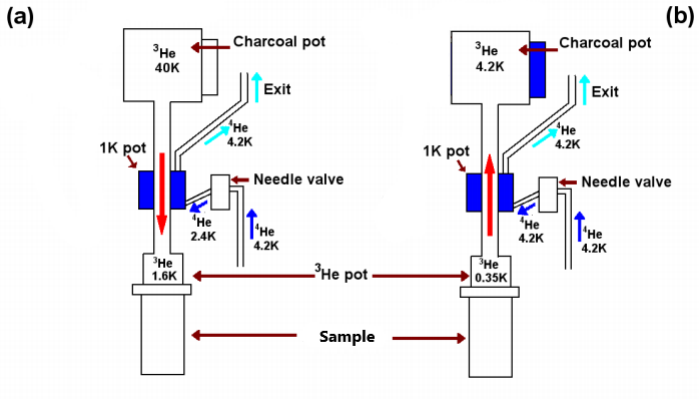

Figure 42: Illustration of the condensation (a) and cooldown phase (b).

Once the insert system is inside the tank the temperature of the sample lowers to 4.2 K as the device thermalizes with the ^{4}He bath and this is helped by the exchange gas.

To further lower the temperature and reach the 300 mK range we need to perform the following procedure, also illustrated in Fig. 42. Inside the central hollow stick, on the upper part, there is a set of active charcoals filled with ^{3}He gas that is fully retained when the charcoals are kept at temperatures lower than 30 K. ^{3}He gas, in contrary to other gasses used, cannot escape the system since it is very expensive and must be recycled during the process. We start

by pumping on the ^{4}He in the 1 K pot with a the scroll pump, whose working principle is illustrated in Fig. 43, backed by a turbo pump. The helium in the

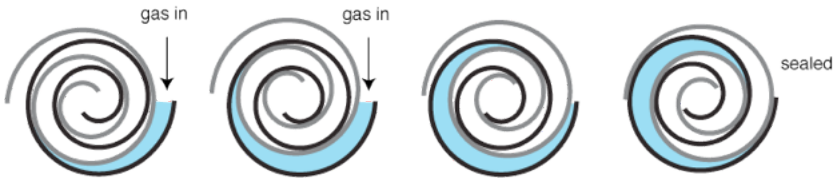

Figure 43: Basic working principle of a scroll pump.

1 K pot is replenished by the capillary visible in Fig. 44 on the bottom of the insert, that sucks it from the helium bath. The temperature of the 1 K pot

Figure 44: Bottom part of the insert system, still uncovered. The floating metal rod on the right is the capillary.

drops below 2 K due to evaporative cooling. The process is controlled by an integrated thermometer, furthermore the apparatus has also a thermometer for the ^{3}He pot (the bottom part of the cold finger in thermal contact with the sample) and a thermometer for the charcoals. At this point the temperature of the charcoals is slowly raised via an integrated heater until it reaches 30 K. The charcoals release the ^{3}He that fills the insert. The ^{3}He gas is now in thermal contact with the 1 K pot and condenses at the bottom of the insert (in the

^{3}He pot) in about 30 minutes. We now stop the heater and the charcoals cool down, reabsorbing the remaining ^3He gas so to effectively reduce the vapour pressure on top of the liquid ^{3}He. The latter again cools via evaporative cooling and since it has a greater equilibrium vapour pressure than ^{4}He, it can reach temperatures below that of ^{4}He at the same conditions.

The minimum temperatures reachable with this setup are in the range of $250 - 300\,\mathrm{mK}$.

4.1.2 Magnet operation

The tank of the cryostat has a built-in superconducting magnet coil that is cooled by the liquid helium present.

The magnetic field is controlled by a current generator controlled externally. Due to the superconducting nature of the magnet, it is possible, once the desired magnetic field value is reached, to disconnect the current generator and let the current flow by itself in the metallic core: this is called persistent mode. To do this a persistent switch is used: when heat is applied, it connects the generator to the magnet. To reconnect the generator it is important to bring it to a current value equal to the one circulating the magnet in persistent mode.

4.2 Lock-in amplifier and wiring

To perform voltage and current measurements, three Stanford Research Systems SR830 lock-in amplifiers have been used. All lock-ins share the same frequency reference.

Fig. 45 shows that the Hall bar contacts are reached through a contact box located at the top of the cryostat.

The hall bar in Fig. 46 can be biased with one lock-in in two ways. One way is voltage bias: we used the lock-in function generator with amplitude settings in the Volt scale and we put in series a voltage divisor (1/1000 or 1/100 depending on the situation) to reach the mV scale. The other way is current bias and the same voltage generator was used but this time we put in series a $10\,\mathrm{M\Omega}$ resistance, in particular we used $1\,\mathrm{V}$ and $1\,\mathrm{M\Omega}$ in series, i.e. a current bias of $100\,\mathrm{nA}$.

The first lock-in was used to measure the current. The second and third lock-in were used to measure four-point voltage drops (V_{xx} and V_{xy}) and their DC voltage sources were used to bias the gate contacts.

The lock-in voltage generators are controllable with a custom built LabView program that allows to perform voltage sweeps between a range of two chosen

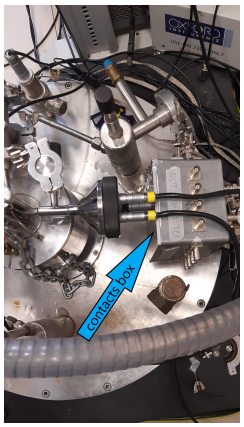

Figure 45: Cryostat contact box.

values.

In the process of changing contacts it is important to keep the Hall bar at ground and also the gates. To do this 50 Ω BNC caps were used.

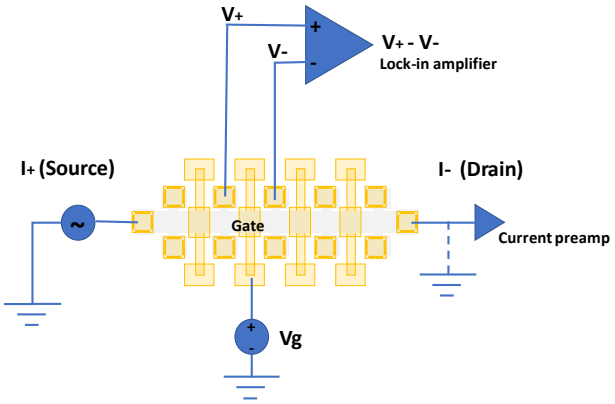

Figure 46: A possible measurement configuration (four-probe measurement). It is possible to measure two voltage differences and bias two gates simultaneously.

It is possible to set the readings representation of the lock-in in two ways. If we imagine a voltage or current measurement as a phasor, we can represent this object in two ways: in the X-Y plane or with polar coordinates R-ϕ. The phase ϕ can be brought to zero or π via an AUTO-PHASE command. As we

will see in chapter 5, since we expect the phase to be constant, we chose to represent voltage and current values with their X component (e.g. V_x or I_x) after performing an autophase on the signal. Another representation is the polar one (e.g. V_R or I_R and V_ϕ or I_ϕ) used in Appendix A.

In the next chapter colored squares over contacts will indicate where the lock-in amplifier was connected to perform voltage measurements.

5

Experimental results

The device on which the measurements have been performed is the Hall bar illustrated in chapter 3. This device serves as proof-of-concept of the Bisector illustrated in chapter 3.

The filters present on the cryostat lines were removed, measurements with filters present are discussed in appendix A.

5.1 Check of the Ohmic contacts

First of all, the device has been mounted on the chip carrier of the Heliox cryostat and then, before inserting the whole insert into the helium bath, a quick check of the sample contacts was performed. Taking as a reference the photo in Fig. 47, we worked in AC current bias using contact 1 and 16 as source and measuring the output current at all the other contacts. We passed 1 V through a bias resistance of 10 MΩ that is much larger than the resistance of the Hall bar, so we expect to measure 100 nA at all probed terminal. All gate contacts have been put to ground. No current was measured flowing through contact 9 and 10. This fact led to the inspection of the sample under the optical microscope, and a lithographic defect was found, so a piece of the Hall bar cut out from the rest of the device (Fig. 47). Due to the Hall bar cut, the only usable gates are two: gate 12 and 14. This is not a big problem since we can perfectly asses the bisection mechanism and use contact 11 as drain.

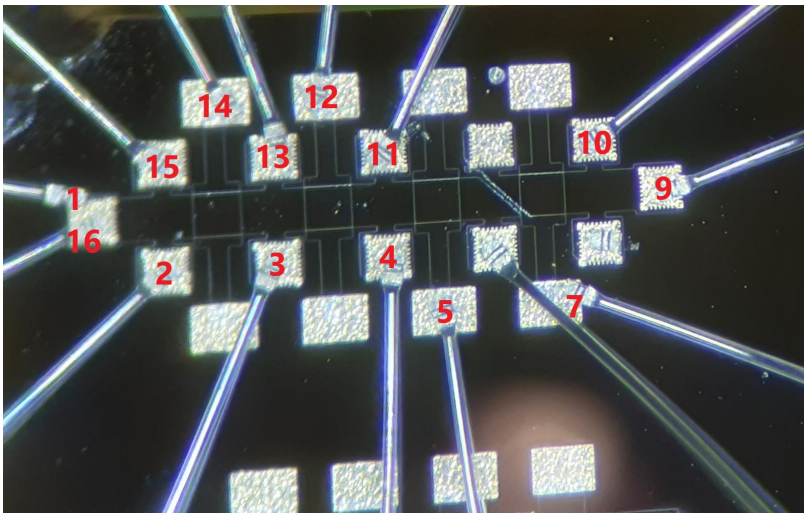

Figure 47: Hall bar device pin out.

5.2 Gates characterization

At this point the sample was inserted in the cryostat helium bath without turning on the magnetic field.

The first measurement that was performed was the characteristics of the two usable gates. We inject 100nA of current at contact 1 together with 16 and measure the output current at contact 11, while sweeping a voltage bias applied to the gate contact. What we call characteristics is a gate voltage sweep while measuring the current on the drain contact keeping source-drain voltage constant. From Fig. 48 can be noticed that the gate characteristics is affected by hysteresis, probably due to charge traps embedded in the substrate [17]. The current pinches off at a voltage gate of $V_g = -0.25\,\mathrm{V}$. When the channel under the gate is depleted, some electrons get trapped and are not injected back at the same voltage value when raising the bias. Fig. 49 shows that the gates behave the same. Hysteresis is dependent on lock-in integration time and temperature, possibly due to the traps having a certain activation energy [18]. The same measurement was performed in Fig. 50 after the condensation cooldown. In Fig. 51, both gates pinch off the currents at $-0.25\,\mathrm{V}$ as also confirmed by a simultaneous bias sweep on both gates.

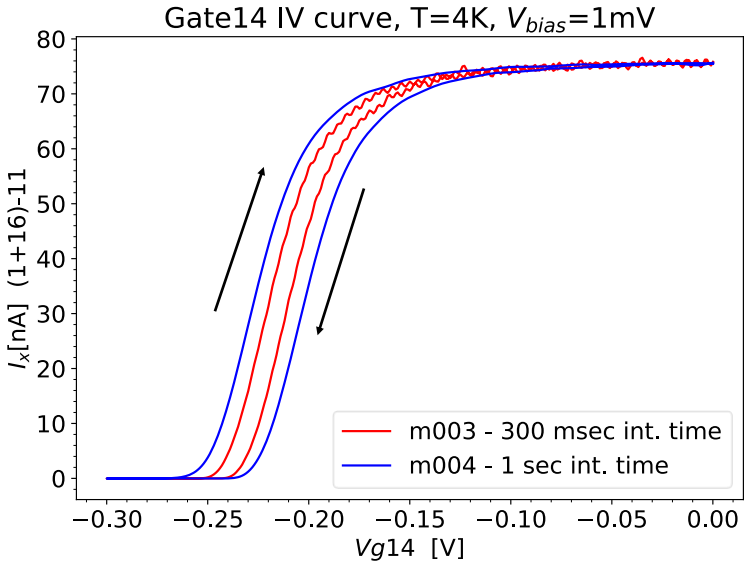

Figure 48: Gate 14 IV curve with different integration times.

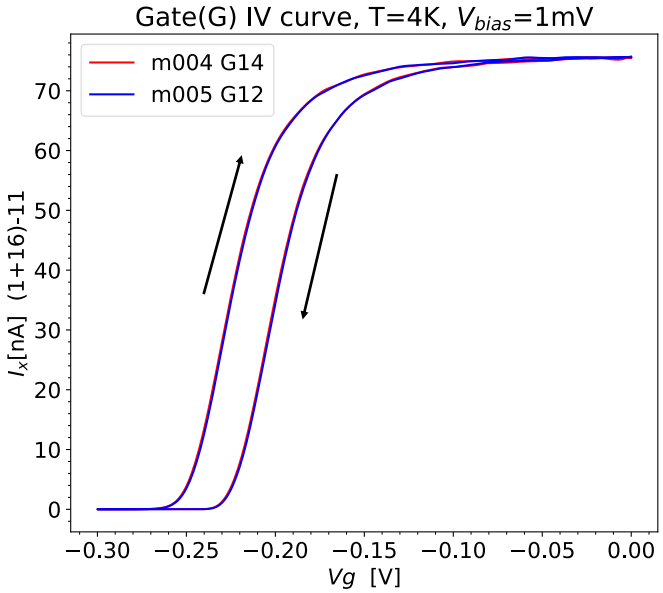

Figure 49: Gate 14 and 12 IV curves with 1s integration time.

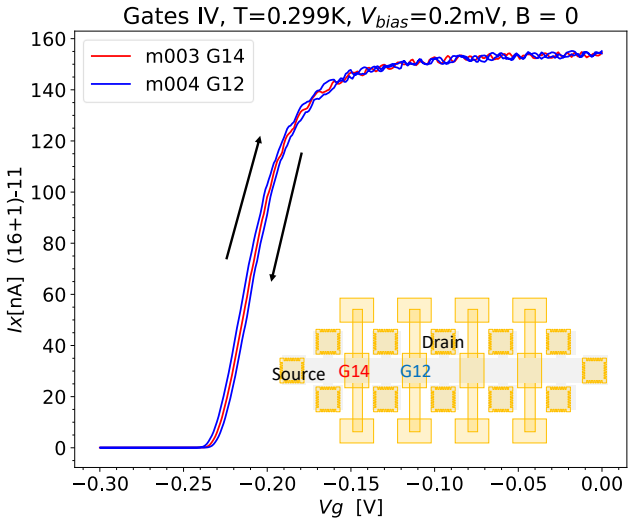

Figure 50: Gate 14 and 12 IV curves.

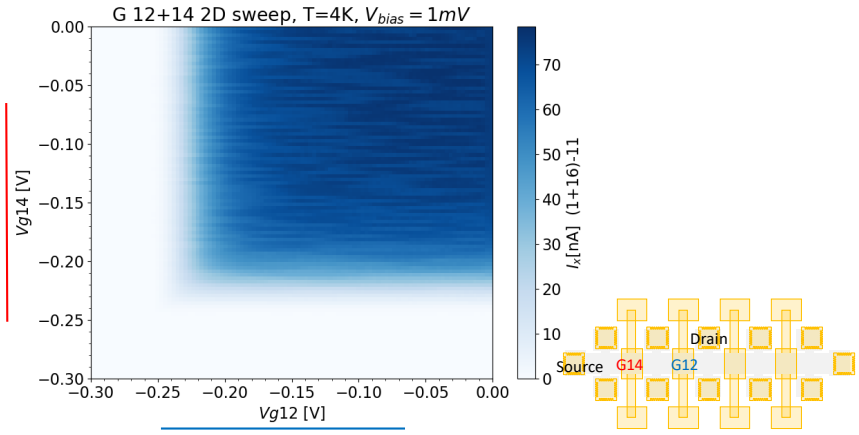

Figure 51: Gate 14 and 12 IV color map.

5.3 2DEG characterization

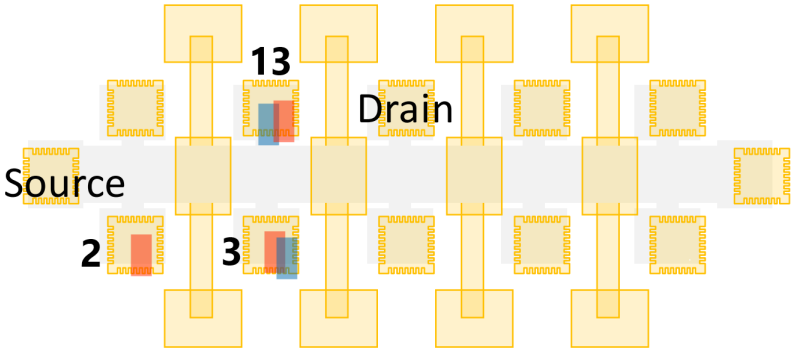

Figure 52: Quantum Hall effect measurement set-up.

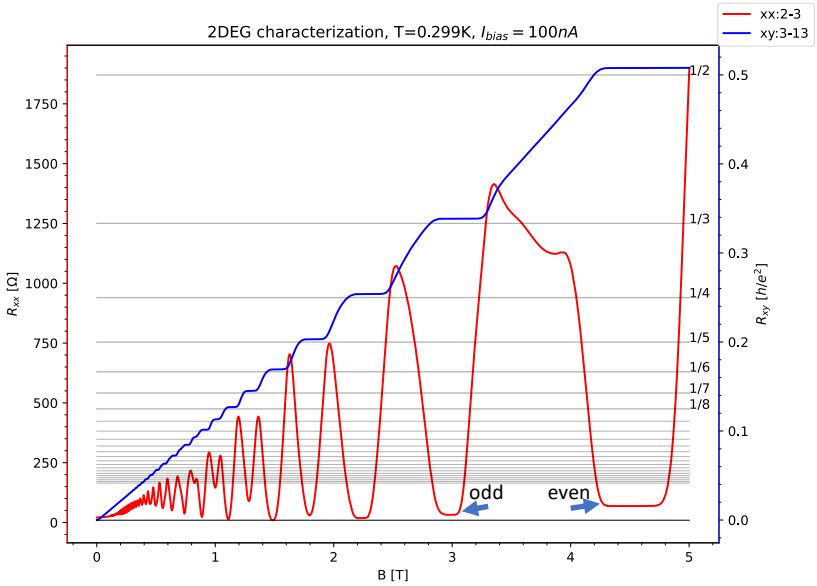

Figure 53: T = 299mK 2DEG characterization.

In current bias and the gates at ground and turning on the magnetic field, we measure the Hall voltage as in Fig. 52, at contacts 3 and 13, and the longitudinal voltage drop along the bar at contacts 2 and 3. Performing the cooldown at 300 mK, we see SdH oscillations visible in Fig. 53, but the quantization at $\nu = 2$

is still not perfect. This is probably due to a parallel conduction occurring under the 2DEG. The quantization ascribable to both spin bands full (even ν) should be sharper than that with only one spin band full (odd ν) because spin band pairs are more separated in energy and better resolved in the case of broadening effects due to a non-ideal sample. The Zeeman splitting is of the order of 0.1 meV, while the Landau splitting is of the order of 0.5 eV. This means that the minimum of R_{xx} for even ν should be lower than that at odd ν. From Fig. 53 we see that this is not the case for the $\nu = 2$ and $\nu = 3$ plateau. The contribution of a parallel conducting layer on R_{xx} resistance increases with the field value [19].

From Fig. 53 we can also find the following transport parameters: electron mobility μ, surface electron density n and the scattering time τ. To do this we use the fact illustrated in chapter 1, that when $B \to 0$ we recover the Drude formulas for ρ_{xy} and ρ_{xx}. The former depend on n and the latter on τ, and so μ from $\rho_{xx} = 1/en\mu$. So what we need to do is finding from Fig. 53 the zero field value of R_{xx} and the slope of R_{xy} curve near the origin (when no plateaus are visible). To convert the measured R values to resistivity ρ values we need to multiply for the ratio between the Hall bar width and height that equals 2.4. The dimensions of the Hall bar are taken from Fig. 54. We find

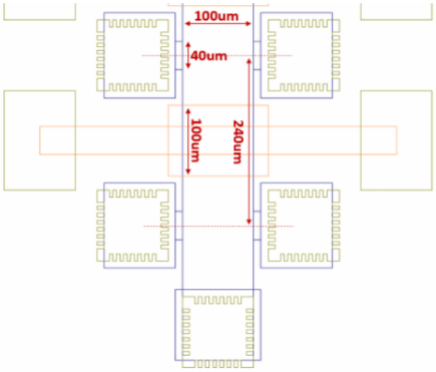

Figure 54: Hall bar size to convert a resistance value to a resistivity.

$\mu = 3.37 \times 10^6\,\mathrm{cm}^2/(\mathrm{Vs})$, $n = 2.2 \times 10^{11}\,\mathrm{cm}^{-2}$ and $\tau = 128\,\mathrm{ps}$.

From better resolved SdH oscillations in the insert of Fig. 55, it was noted that the low field oscillations were characterized by beatings.

We suggest that these beatings originate from a zero field spin splitting interaction (spin orbit interaction) and on this assumption we verify the model

illustrated. In Fig. 56, a fast Fourier transform was applied to the SdH signal

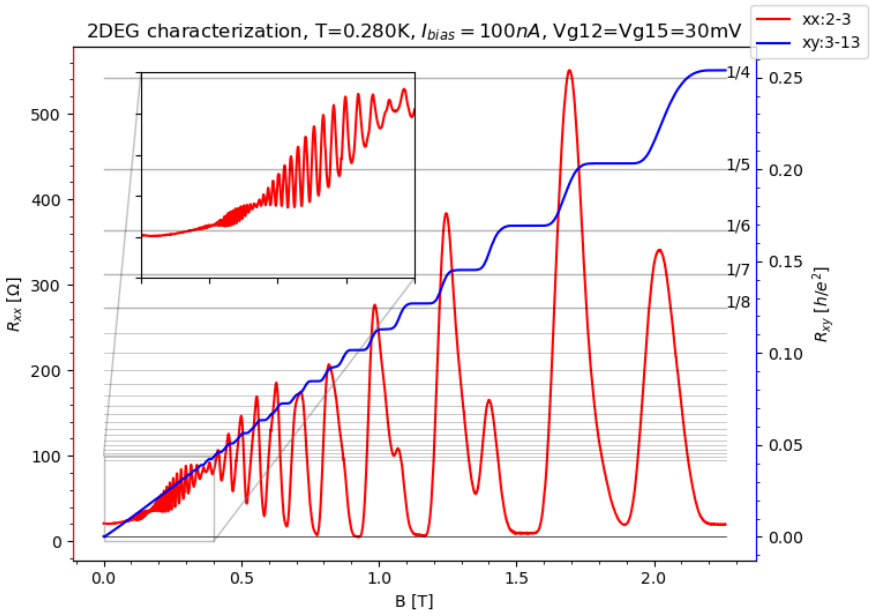

Figure 55: High resolution SdH oscillations with low field beatings zoom in the insert.

to highlight the various frequencies responsible for the main oscillations and the low field beatings. From the fit in Fig.57, using the model in [20], it is possible to get the following values: the effective gyromagnetic ratio of the electron and the zero field spin splitting. From the spectrum of the Hamiltonian (1.14) taking into account also Zeeman effect and Rashba spin-orbit coupling, one finds that the energy difference between levels with spin up and spin down is $\delta = [(E_L - E_Z)^2 + \delta_0^2]^{1/2} - E_L$. E_L is the Landau level spacing $\hbar\omega_c$, E_Z is the Zeeman splitting $g^* B \mu_B$ and δ_0 is the zero field spin splitting. To perform a fit on the experimental data we know that δ takes a special form for the field values at which SdH oscillations present a beating node, in particular $\delta = \eta\hbar\omega_c$, where ω_c is the cyclotron frequency at beating node field value and $\eta = 0.5, 1.5, 2.5, ...$ from the highest to the lowest field value. It is found that $g^* = -0.29 \pm 0.06$ and $\delta_0 = 0.638 \pm 0.007$ meV. For bulk GaAs $g^* = -0.44$ [21], but here the value is higher due to the presence of the heterostructure quantum well that confines electrons [22–25]. This effect has been used to engineer the g^* factor [26, 27].

From these parameters and the transport parameters it is possible to reconstruct the SdH curve with the model from [20]. Comparing Fig. 58 and Fig. 59,

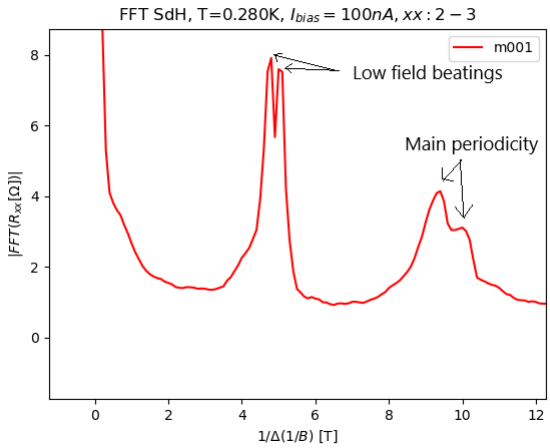

Figure 56: FFT of the SdH signal in Fig. 55.

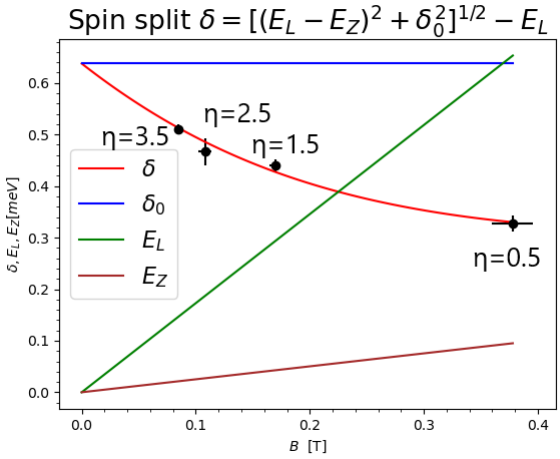

Figure 57: Spin splitting model fit. The red curve takes into account Zeeman, Landau and zero field (SO) splitting, the other curves are the isolated spin splitting contributions. E_L, E_Z and δ_0 are respectively Landau, Zeeman and zero field spin split.

the last experimental beating appears damped compared to the theoretical one, presumably due to too short acquisition time.

Other effects from which this beating pattern can emerge have been studied in quantum well systems with more subbands occupied [28–30].

After these measurements we set the magnetic field at a value corresponding

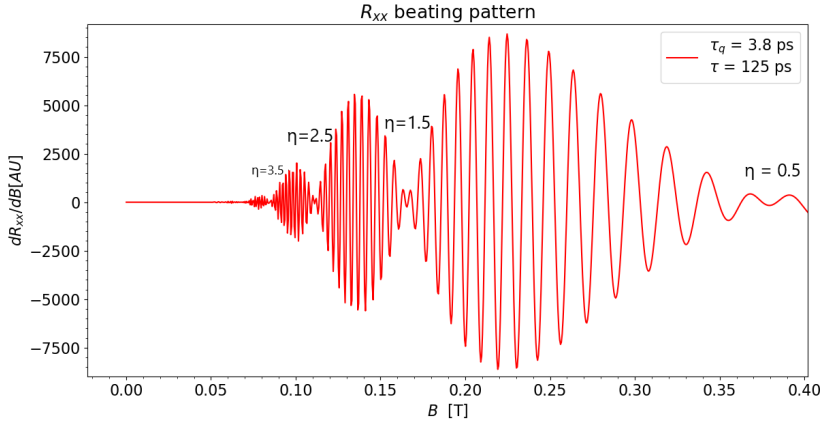

Figure 58: Theoretical SdH curve (model from [20]) differentiated with respect to the magnetic field to remove DC components. τ_q is the quantum scattering time (Landau level line width) and was chosen to better match the experimental figure.

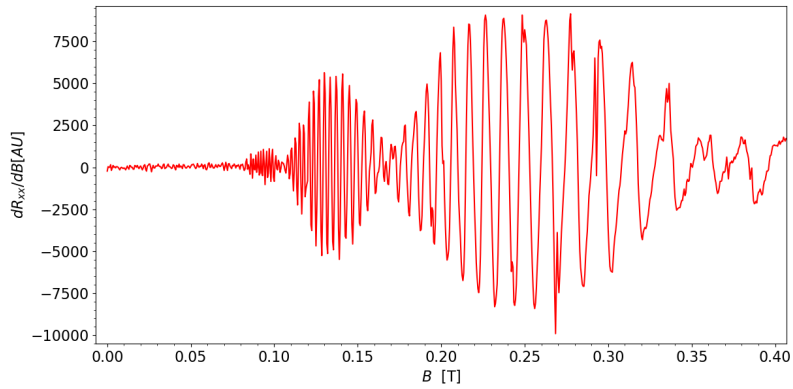

Figure 59: Experimental SdH curve differentiated with respect to the magnetic field.

to the $\nu = 2$ center of the R_{xy} plateau, that is $B = 4.6\,\mathrm{T}$.

5.4 Chirality check

To determine the chirality of the edge current when turning on the magnetic field at a certain ν value, contact 4 is left floating and current is measured at

contact 11 as in Fig. 60. For positive magnetic field value, non-zero signal was measured, instead if we ground contact 4, no signal is measured at contact 11. If we measure current at contact 4 while keeping contact 11 grounded or floating, no difference was detected. This means that for positive field values we have anticlockwise chirality.

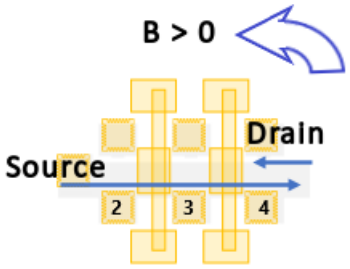

Figure 60: Counterclockwise chirality for B $>$ 0. In this figure the Drain is at contact 11.

5.5 Gate characteristics at $\nu = 2$

Now we perform a series of voltage measurements using the contacts across a gate (along the Hall bar or in diagonal), with various combinations while varying the gate voltage bias or the filling factor underneath. All of this is to study the bisection effects illustrated in chapter 3.

We bias the Hall bar with $V_b = 0.2\,\mathrm{mV}$ using the Source and Drain contacts illustrated in Fig. 61. For the voltage along the device and across the gate 14 (xx), what we observe in Fig. 61 agrees with the behaviour studied in section 2.4.1, except for the fact that the values on the plateau appear shifted due to $R_{xx} \neq 0$.

The same type of measurement but along the gate (xy), was performed. The correct behaviour is observed also in this case but again the plateau values are shifted and we do not precisely have $-V_b$ at $\nu = 2$ (again Fig. 61).

In Fig. 62, the same is repeated on gate 12 and with other contacts on gate 14.

Now we also measure the voltage across the diagonal contacts of the gate. And again, we see from Fig. 63 the correct behaviour and shifted values.

Now we measure the case with two barriers at $\nu = 1$. The diagonal voltage

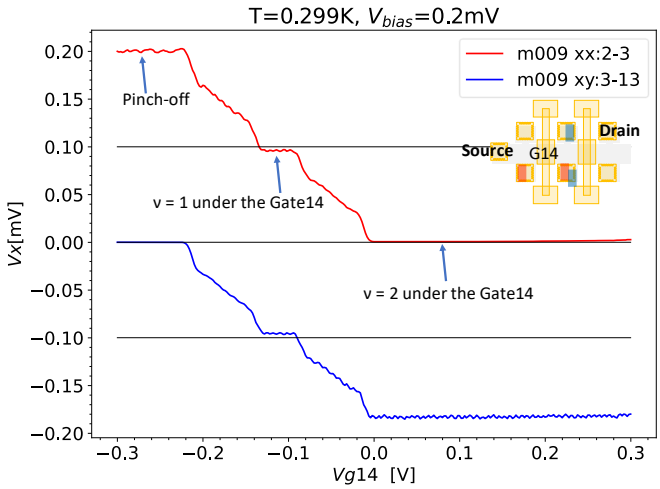

Figure 61: Gate 14 bias sweep and voltage measurement along the device (xx) and along the gate (xy).

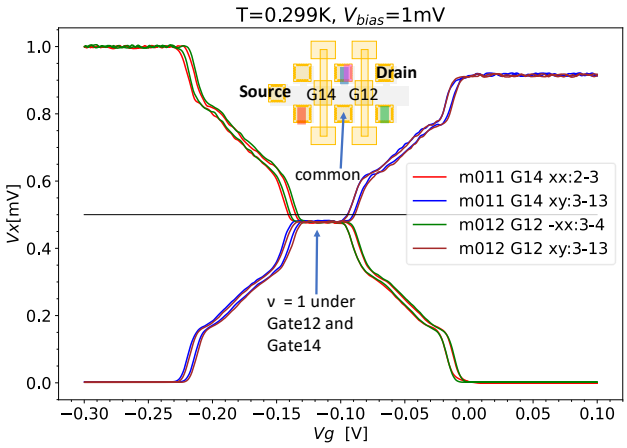

Figure 62: Gate14 or Gate12 bias sweep and voltage measurement along the device (xx) and along the gate (xy). Bilateral sweep of gate voltage was performed and hysteresis is visible.

drop and the longitudinal voltage drop measured in Fig. 65 agrees with the theoretical values, up to the usual offset due to the non-vanishing R_{xx}.

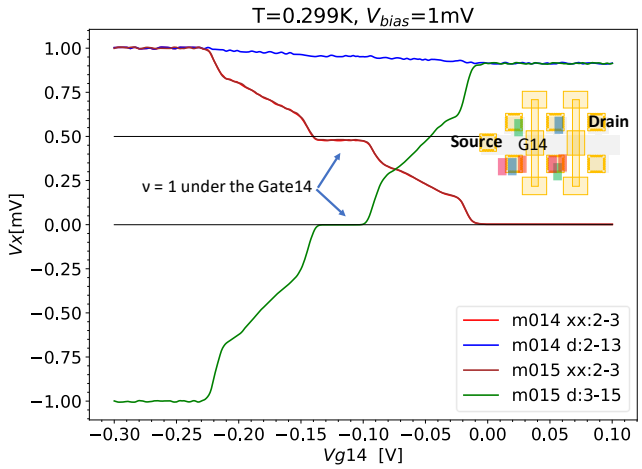

Figure 63: Longitudinal voltage drop and diagonal voltage measurements on gate 14. A non-zero slope is visible on the blue curve

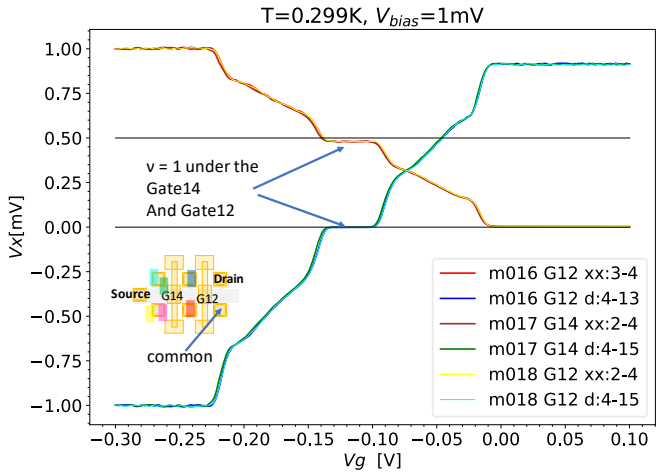

Figure 64: Same as Fig. 63 but also on gate 12 and with different contacts. The gates exhibit no significant difference in operation.

At this point the only thing left to measure the voltage drops in all possible barrier configurations. This has been done in Fig. 66 and Fig. 67, where a 2D

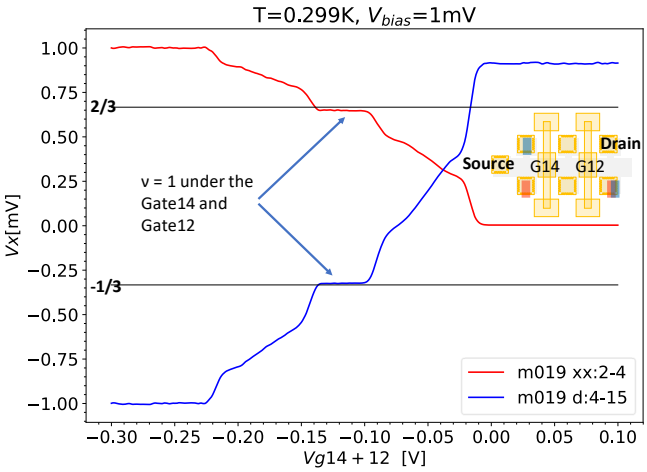

Figure 65: Simultaneous sweep on both gate voltage biases; diagonal and longitudinal measurements crossing both gates.

colour map was made by performing a 2D sweep on the voltage bias of both gates.

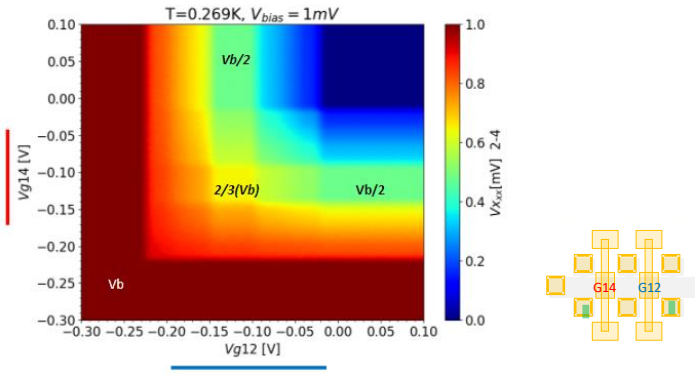

Figure 66: 2D map of the longitudinal voltage drop across the two barriers. Theoretical values are written on the respective plateaus.

Apart from the discrepancies in Fig. 61-65, we correctly obtain the working regimes of the device.

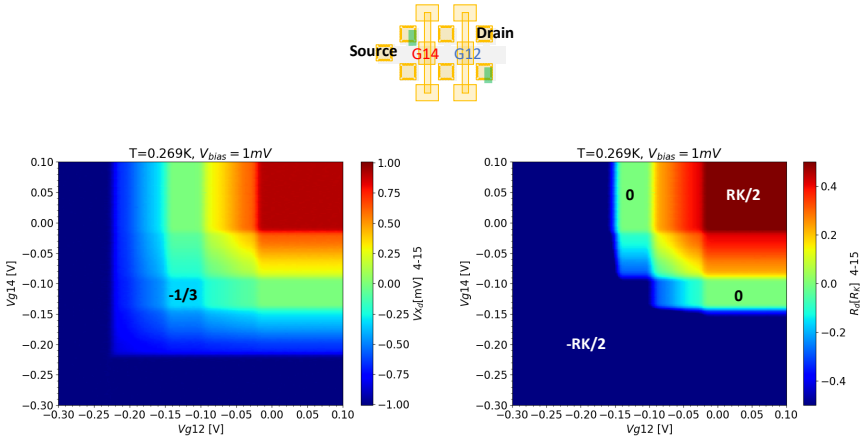

Figure 67: 2D map of a diagonal voltage across the two barriers. On the left the colors represent voltage values, on the right diagonal resistance. Theoretical values are written on the respective plateaus.

5.6 Gate characteristics at $\nu = 4$

Now we study the case of the Hall bar at $\nu = 4$. This case is interesting because the bisection can also be achieved at $\nu = 4$ with a barrier at $\nu = 2$.

We bring the magnetic field to $B = 2.26\,\mathrm{T}$. This value is an average between the center of the $\nu = 4$ R_{xx} and R_{xy} plateaus. This time we expect a larger spectrum of voltage bias fractions observable.

Using a single barrier, we can observe four plateaus in Fig. 68, but the fractions visible are still the same on the diagonal (the last row of Table 2 of section 2.4.3). New fractional values (the last row of Table 1 of section 2.4.3) are visible along the sample contacts across the barrier in Fig. 69. The fractions that actually appear on the plateaus of the red curves are not quite the theoretical ones and this is due to the non-vanishing R_{xx}.

Other fractions in Fig. 70 and Fig. 71 (diagonal of Table 1 and Table 2 in section 2.4.3) emerge measuring voltages across both barriers on different states.

It is also possible to measure all possible combinations performing a 2D sweep on both gate bias voltages as previously seen. Table 1 and Table 2 in section 2.4.3 include all values obtainable in principle in the measurements shown in Fig. 72 and Fig. 73.

From all plots shown we correctly distinguish the predicted plateaus. Even

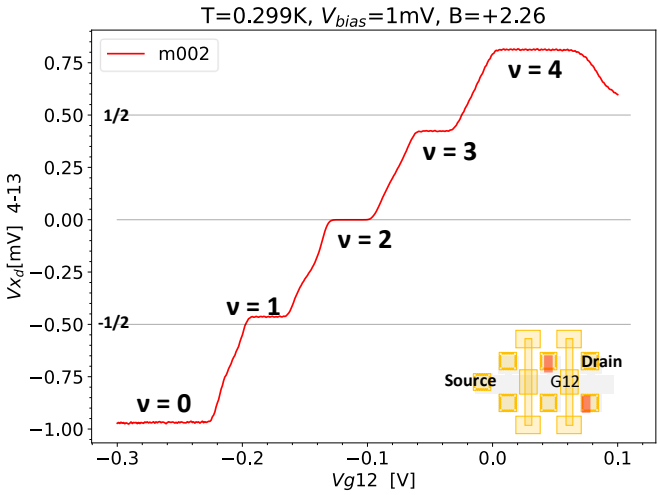

Figure 68: Gate12 diagonal voltage vs gate12 voltage bias with theoretical V_b fractions.

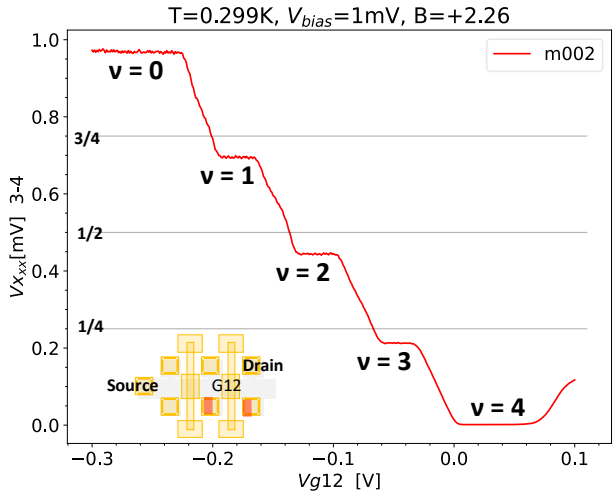

Figure 69: Gate12 longitudinal voltage drop vs gate12 voltage bias with theoretical V_b fractions.

if their voltage values are not the ones we expected for a sample with $R_{xx} = 0$, we can now be sure that the bisection scheme works correctly at different filling

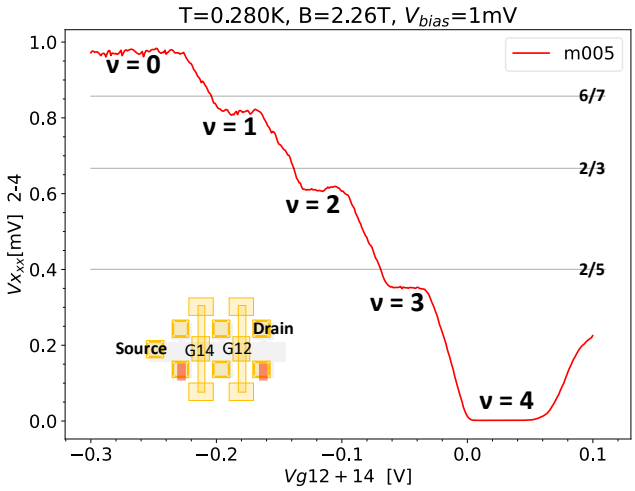

Figure 70: Longitudinal voltage drop across both vs gate12 and gate14 voltage bias with theoretical V_b fractions (diagonal of Table 1 in section 2.4.3).

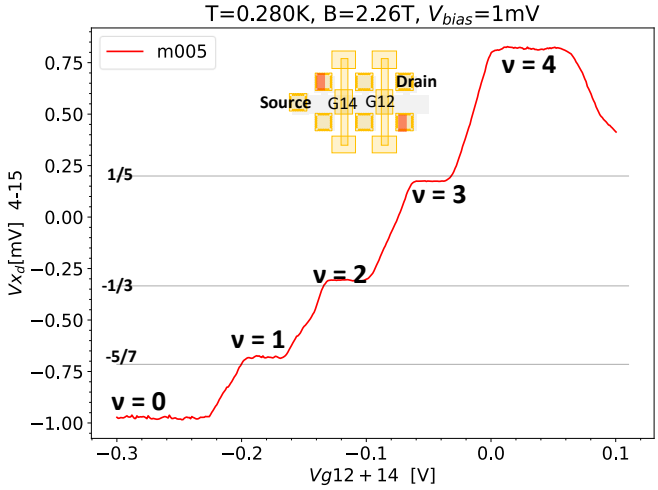

Figure 71: Diagonal voltage across both vs gate12 and gate14 voltage bias with theoretical V_b fractions (diagonal of Table 2 in section 2.4.3).

factors. Thus, it is possible to study QH breakdown effects on this Hall bar device to obtain voltage bias values for a safe operation, even for the full bisector.

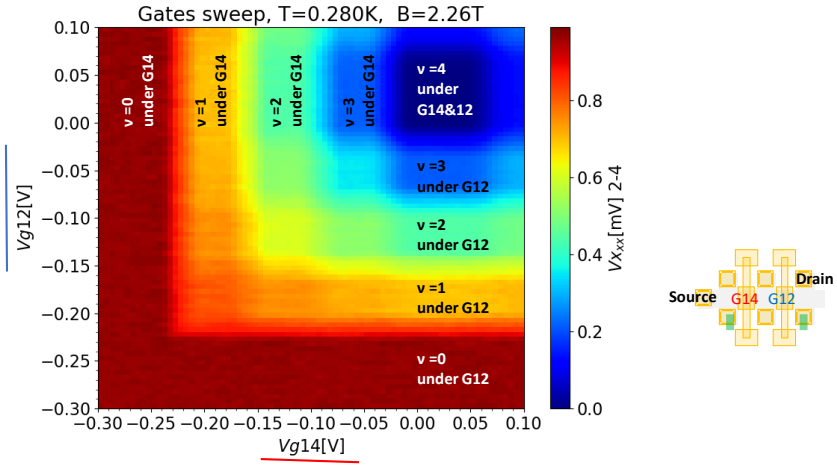

Figure 72: Longitudinal voltage drop across both vs 2D gate voltage bias.

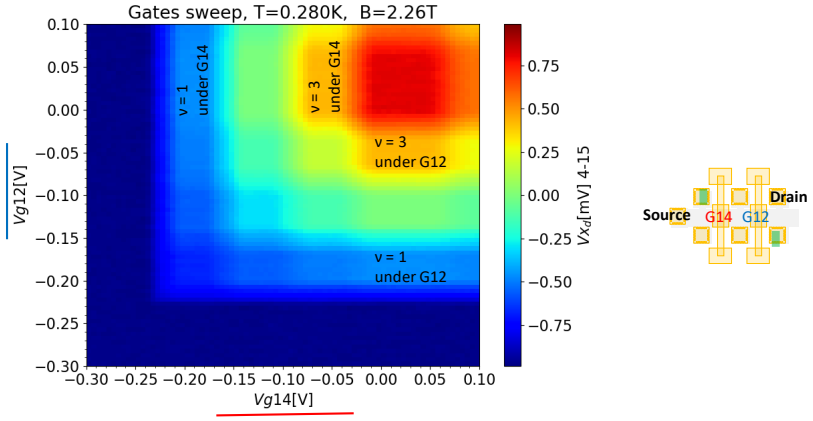

Figure 73: Diagonal voltage across both vs 2D gate voltage bias.

5.7 Quantum Hall breakdown

The breakdown of the QHE in conventional Hall bars is an important limit to the ultimate metrological precision of this class of resistance standards. Given the finite intrinsic current and voltage noise of any measurement system, ideally one would like to measure a quantum Hall resistance using the largest possible currents and voltages. On the other hand, the precise quantization of resistance

relies on the fact that the bulk is almost perfectly insulating, and this condition fails when the Hall voltage exceeds a limit voltage leading to a breakdown of the QHE [31–33]. For this reason, it is generally important to quantify the breakdown voltages of this class of devices.

The breakdown of the QHE can derive from a the large number of interplaying mechanisms [34–36]. In the case of a simple Hall bar, the breakdown voltage can be typically increased by fabricating a wide Hall bar, so that the voltage drop is distributed across the large lateral dimension of the Hall bar.

The presence of a top gate complicates the situation. For instance, in order to achieve a $\nu = 1$ condition under a barrier, a well-defined gate voltage has to be applied to the gate, with respect to the channel. If the transverse voltage drop in the channel becomes large, it is clear that it is not possible to use a field-effect electrode to induce a uniform carrier density in the channel, and the voltage drop within the channel influences the effect of the gate. This kind of effects is generally referred to as "self-gating".

We now study the voltage bias range at which the device can operate before the breakdown occurs, since we expect to find deviations from the values reported in literature for conventional Hall bars. To do this, we position ourselves on various plateaus on the diagonal voltage of a certain gate and increase the voltage bias while sweeping on the plateau. What we expect to see is the shrinking of the plateau with increasing voltage and its disappearance at a certain voltage value. We would like to give an estimation of this critical voltage value, where the quantum Hall effect breaks down. The figures 74 to 78 are measurements at different Hall bar ν and different ν diagonal plateau under the gate (indicated by a blue arrow on a V_d vs V_{gate} plot at a fixed bar bias).

To estimate the voltage at which the breakdown happens, the following procedure was put in place. In every QH breakdown color plot there is a colored triangular region that represent the shrinking of the plateau. For every V_{bias} value, the corresponding V_{d_X} values stay constant inside the triangular region, up to a certain fluctuation. When we approach the region boundary the fluctuation increases and as soon as it does we define there a scatter point with an error bar that covers the region with this increased fluctuation. A linear fit was performed on these points as an approximation to estimate the breakdown voltage value, this value is the intersection of the fitting lines i.e. when the diagonal plateau disappears. The result is shown in Fig. 74 to Fig. 83. Thus we can deduce that the device safely works at $\nu = 2$ and at $\nu = 4$ for bias

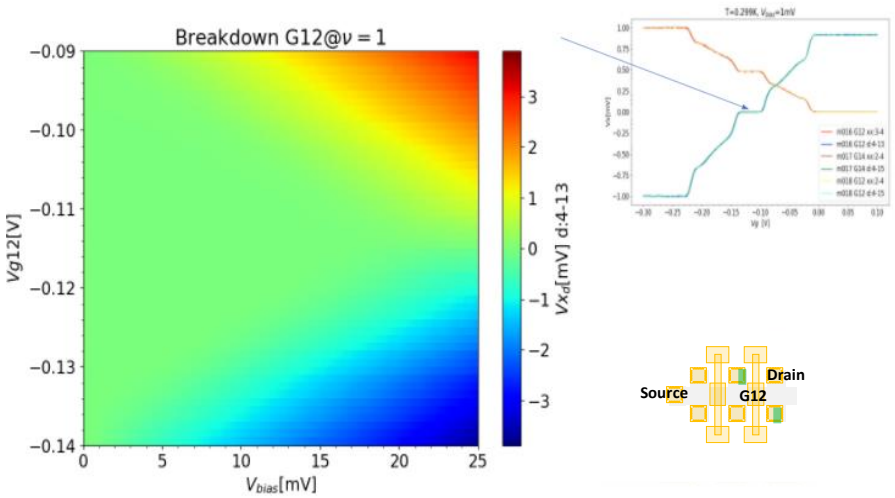

Figure 74: Breakdown measurement with the Hall bar at $\nu = 2$ and sweep on the $\nu = 1$ diagonal plateau. The green region is the shrinking plateau.

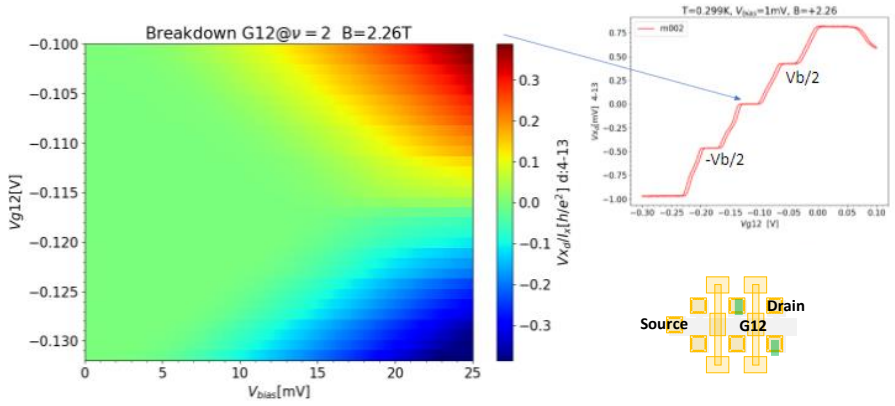

Figure 75: Breakdown measurement with the Hall bar at $\nu = 4$ and sweep on the $\nu = 2$ diagonal plateau. The green region is the shrinking plateau.

voltages respectively lower than 20 mV and 10 mV; they are of the same order of the plateau maximum extension in V_g.

From the voltage values obtained we could find the corresponding critical currents from the Drain measurement, the error bar on the current is found from the two corresponding extremal voltage values. For Fig. 74, i.e. one bar-

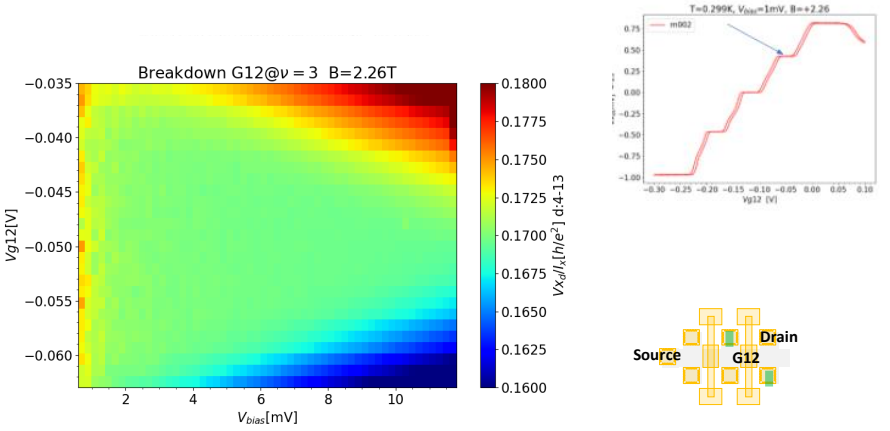

Figure 76: Breakdown measurement with the Hall bar at $\nu = 4$ and sweep on the $\nu = 3$ diagonal plateau. The green region is the shrinking plateau.

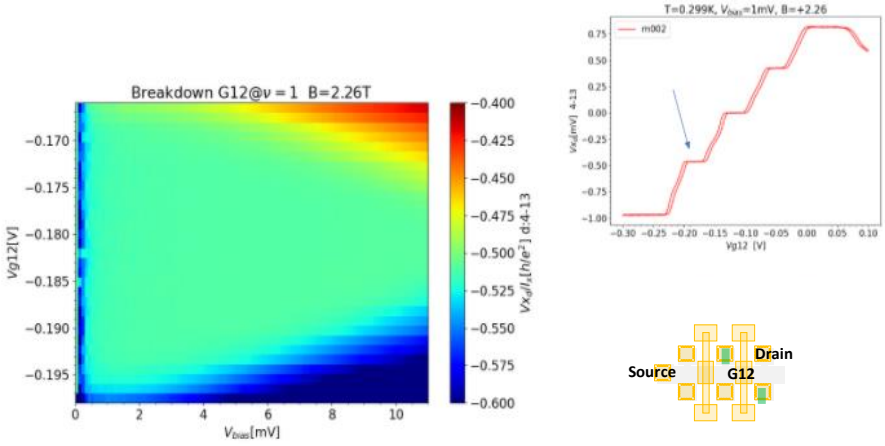

Figure 77: Breakdown measurement with the Hall bar at $\nu = 4$ and sweep on the $\nu = 1$ diagonal plateau. The green region is the shrinking plateau.

rier at $\nu = 1$ and the bar at $\nu = 2$, we find $I_c = 0.794 \pm 0.008\,\mu$A, this value is low compared to standard Hall bars used for metrology [37], where current bias of the order of the $10\,\mu$A are used to achieve high precision and I_c can be of the order of $100\,\mu$A. This low value I_c is possibly due to the self-gating effect discussed previously. Examples in literature of a low I_c is found in the

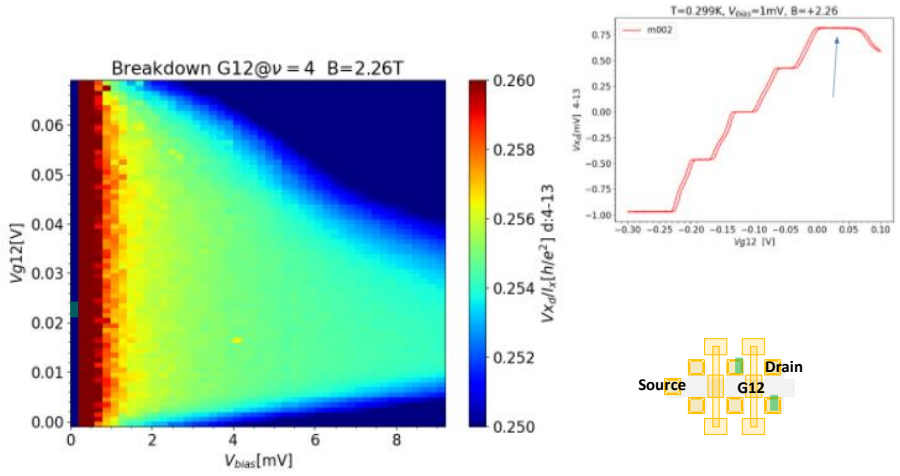

Figure 78: Breakdown measurement with the Hall bar at $\nu = 4$ and sweep on the $\nu = 4$ diagonal plateau. The green/cyan region is the shrinking plateau.

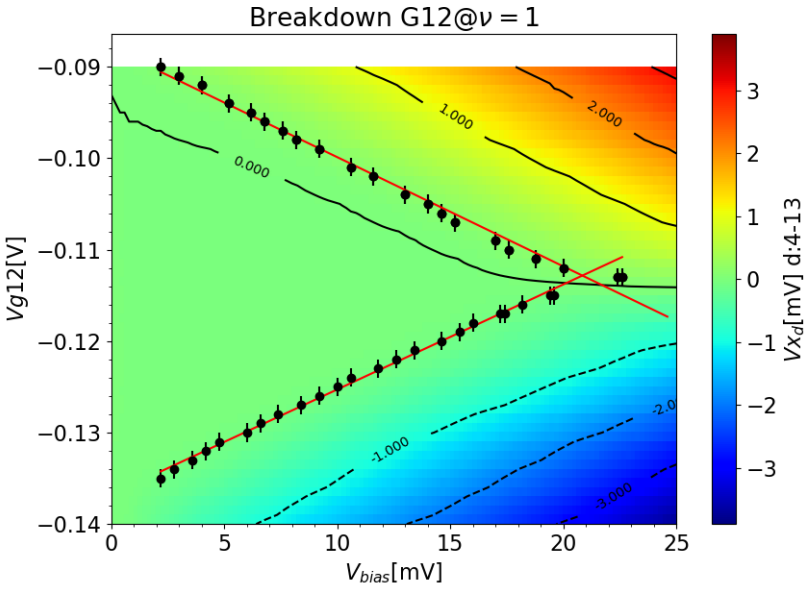

Figure 79: Fig.74 fit. $V_{breakdown} = 20.8 \pm 0.2\,\mathrm{mV}$.

effect of a disordered or corrugated sample [38] [39]. The non zero value of R_{xx}, though not contributing so prominently in our case, can also decrease I_c as it

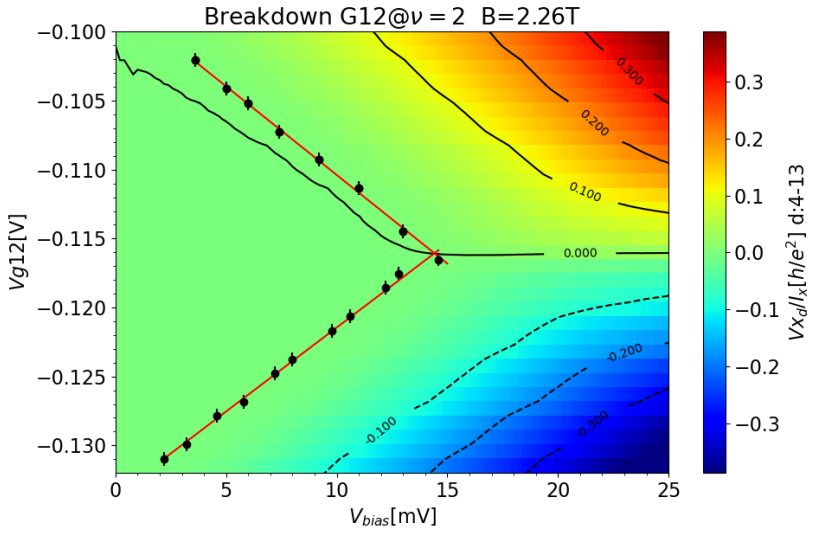

Figure 80: Fig.75 fit. $V_{breakdown} = 14.4 \pm 0.2\,\mathrm{mV}$.

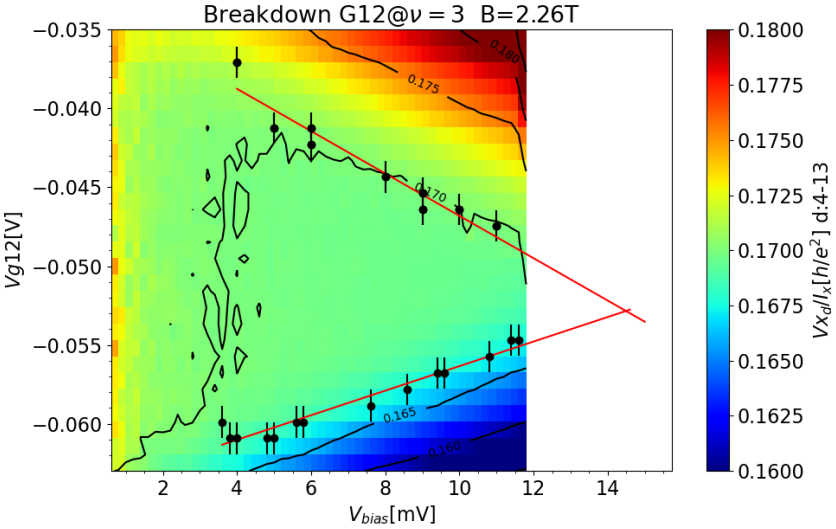

Figure 81: Fig.76 fit. $V_{breakdown} = 15 \pm 1\,\mathrm{mV}$.

introduces more dissipation effects. For other values of I_c from the Fig. 80 to Fig. 83 we can only give an order of magnitude since the preamp did not have current range settings for $I > 1\,\mu\mathrm{A}$ and it was challenging to measure high

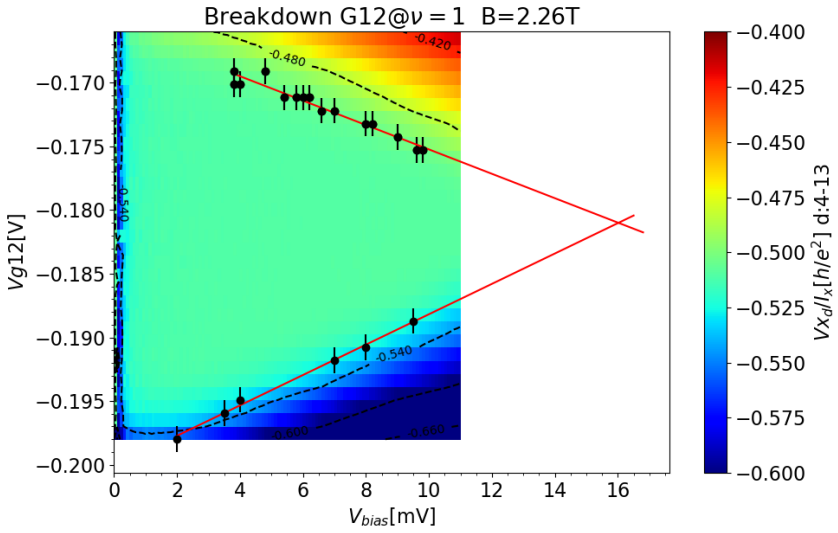

Figure 82: Fig.77 fit. $V_{breakdown} = 16.0 \pm 0.6\,\mathrm{mV}$.

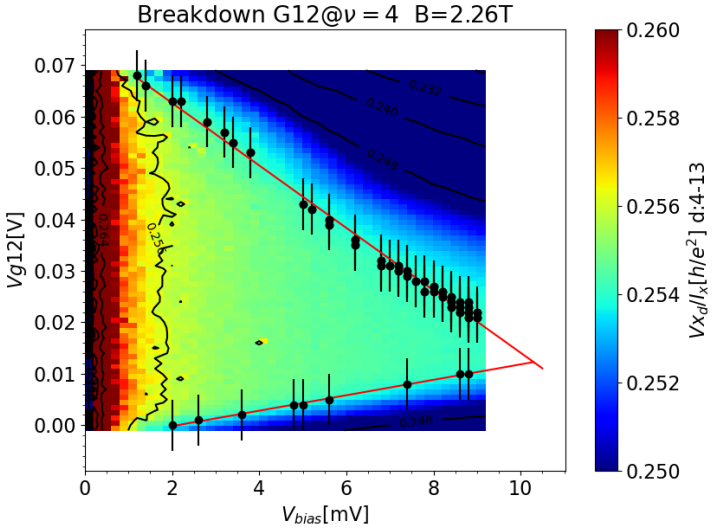

Figure 83: Fig.78 fit. $V_{breakdown} = 10.3 \pm 0.1\,\mathrm{mV}$.

voltage bias without the lock-in saturation, but it is possible to give an order of magnitude considering the currents measured before the preamp saturation. For one barrier at $\nu = 2$ and $\nu = 1$ we find $I_c \gtrsim 0.3\,\mu\mathrm{A}$ and for $\nu = 3$ and

$\nu = 4$ we find $I_c \gtrsim 1\,\mu$A. For lower ν values under the gate find a lower I_c. The value of I_c is also linked to the width of the bar and so one should not expect significant deviations in I_c using the Bisector. The case with the Hall bar at $\nu = 2$ and one barrier at $\nu = 1$ has a higher breakdown voltage value than all the cases with $\nu = 4$, this is possibly due to the effective restriction of the insulating bulk due to more edge channels present, in fact we notice that there is a general decrease of the breakdown voltage values for the Hall bar at $\nu = 4$ with increasing ν under the gate.

To summarize, we can say that we find a breakdown bias voltage of the order of 10 mV, instead of the order of 1 V for conventional Hall bars. This means that for metrological applications the signal to noise ratio will be 100 times inferior. So the flexibility of the circuit limits the precision achievable, but this does not mean that the device will not be useful for calibrations as it actually depends what precision we want to reach and, furthermore, the ultimate precision of the device is still unknown.

6

Output resistance

All measurements reported in this thesis have been obtained using a four-probe technique, that allows to remove the effect of contact resistances and to obtain a precise QH measurement: this is certainly true as long as voltage probes do not drain any current, i.e. the measurement apparatus has to have a large internal resistance (infinite in the ideal case).

In this chapter we discuss deviations due to non-ideal effects in the measurement configuration and, in particular, to the non-zero output resistance R_{out} of the studied QH circuits. The calculation of R_{out} is not very simple in the QH regime [5, 9], and the results of a numerical study will be reported in the first part of the chapter. In the second part, a resistive model will be proposed to describe the behaviour of the studied QH circuits. The quantity R_{out} must be taken into account when assessing the ultimate precision of our devices, as it perturbs the fractional values of R_K derived from the bisection scheme.

To see the effect of a finite R_{out}, now we consider the simple one barrier circuit illustrated in Fig. 84 and Fig. 85 working at $\nu = 2$. To perform a four-probe measurement we choose two contacts to inject a known current and two contacts where to measure a voltage drop. Fig. 84 and Fig. 85 show a limit where an ideal voltage measurement (thus draining no current) is used to measure $V = V_+ - V_-$.

Now we illustrate how to write the equations to calculate voltage drops on this kind of circuits, following the Landauer-Büttiker formalism: each edge channel carries an excess current V_c/R_K, where V_c is the voltage of the contact from which the edge originates. For the circuit in Fig. 84 we write the current

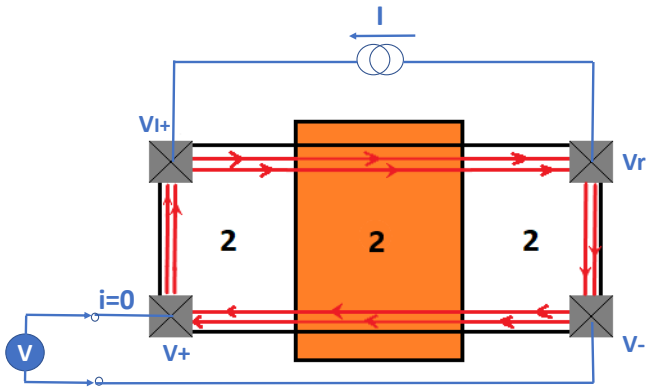

Figure 84: One barrier Hall bar at $\nu = 2$. Barrier at $\nu = 2$ and ideal voltage measurement (the voltage probe drains no current).

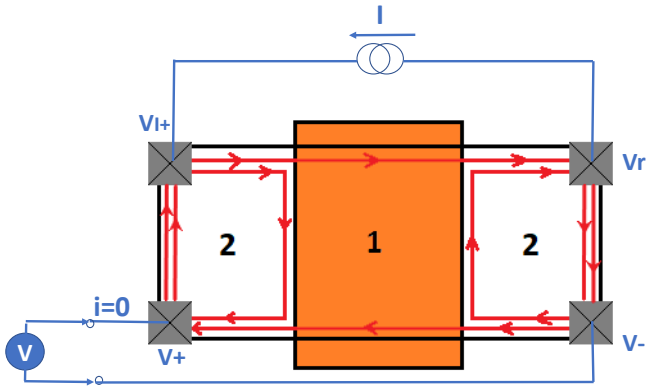

Figure 85: One barrier hall bar at $\nu = 2$. Barrier at $\nu = 1$ and ideal voltage measurement (the voltage probe drains no current).

conservation for each contact:

$$\begin{cases} 2V_+ + IR_K = 2V_{I+} \\ 2V_{I+} = 2V_r + IR_K \\ V_r = V_- \\ V_+ = V_- \end{cases} .$$

For the one in Fig. 85 we write for each contact:

$$\begin{cases} 2V_+ + IR_K = 2V_{I+} \\ V_{I+} + V_- = IR_K + 2V_r \\ V_r = V_- \\ V_{I+} + V_- = 2V_+ \end{cases} .$$

We can generalize the two cases by introducing the parameter $b = 2 - \nu$, that is equal to $b = 0$ for a barrier at $\nu = 2$ and $b = 1$ for the barrier at $\nu = 1$. The new equations read:

$$\begin{cases} 2V_+ + IR_K = 2V_{I+} \\ (2-b)V_{I+} + bV_- = IR_K + 2V_r \\ V_r = V_- \\ bV_{I+} + (2-b)V_- = 2V_+ \end{cases} .$$

From here we can find a resistance $R = V/I = (V_+ - V_-)/I = bR_K/2(2-b)$ for both cases. However, if our measuring apparatus has an internal resistance R_{load}, we have to take into account a current i drained from the measurement contacts (Fig. 86 and Fig. 87). In this last case we proceed in a similar way, taking into account also the new current i. The generalized equations are:

$$\begin{cases} 2V_+ + IR_K = 2V_{I+} \\ (2-b)V_{I+} + bV_- = IR_K + 2V_r \\ 2V_- + iR_K = 2V_r \\ bV_{I+} + (2-b)V_- = 2V_+ \\ V_+ - V_- = iR_{load} \end{cases} . \tag{6.1}$$

Now the voltage we read is perturbed to be $V + \delta V$, where V is the open circuit voltage (ideal case). Note that now $V + \delta V = V_+ - V_-$. The voltage

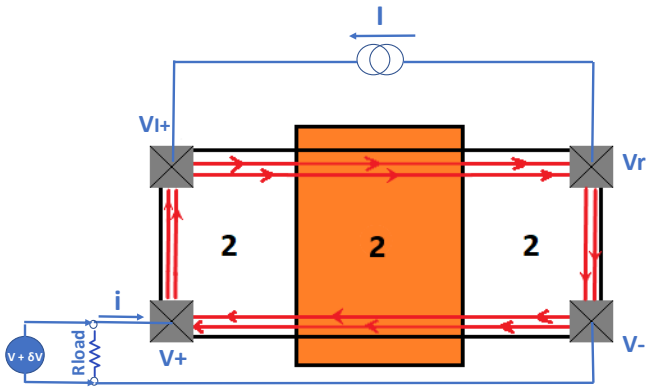

Figure 86: One barrier Hall bar at $\nu = 2$. Barrier at $\nu = 2$ and a voltage probe with a finite internal resistance.

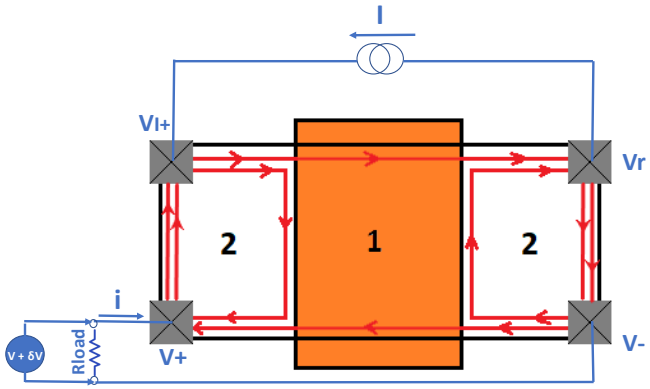

Figure 87: One barrier Hall bar at $\nu = 2$. Barrier at $\nu = 1$ and a voltage probe with a finite internal resistance.

$V + \delta V = V - iR_{out}$ and so $\delta V = -iR_{out}$.

Since $R = V/I$, we have $i = V/(R_{load} + R_{out})$. The resistance R is then perturbed as:

$$\frac{V + \delta V}{I} = R\frac{R_{load}}{R_{load} + R_{out}}$$

If $R_{load} \gg R_{out}$ we recover the ideal case and so that is why it is important to study the behaviour of R_{out}. The value of R_{out}, as a function of the number of stages and their configuration, can be investigated numerically and with an analytical model for the Bisector.

6.1 Numerical estimate of R_{out}

We consider now the device studied in section 2.4.5. In this case, $V_+ = V_{L,0}$, $V_- = V_{R,n}$ and $R = V/I = (V_+ - V_-)/I = kR_k/2^{n+1}$ (for ideal measurement), where n is the number of stages of the bisector and k is integer and depends on the lateral barrier configuration. Now we study what happens when we perform a non-ideal measurement on this QH device (Fig. 88), in particular we calculate R_{out}. We will do this for a generic n.

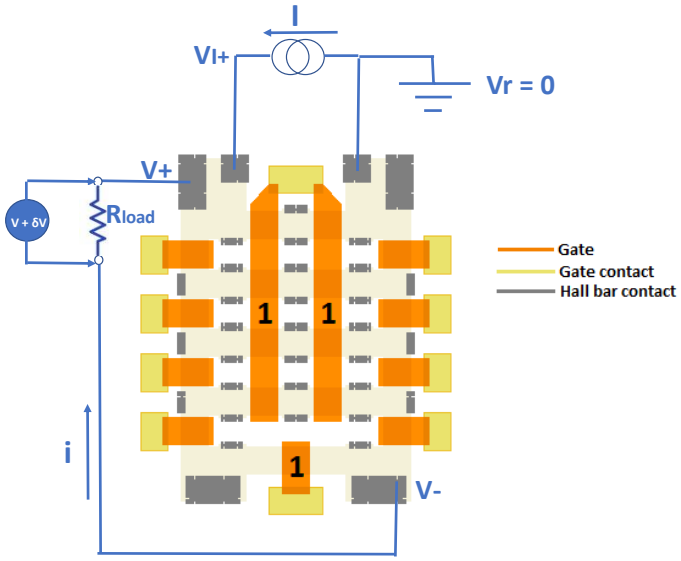

Figure 88: Four ($n = 4$) stages bisector. A non ideal measurement is performed on the contacts yielding the R_K fractions studied in 2.4.5.

To find R_{out} we need to know the perturbed voltage drop $V + \delta V = V_+ - V_-$ and the current i. To do this we write at every Hall bar contact of the device equations like in 6.1 (the central barriers visible in Fig. 88 are always kept at $\nu = 1$) and to solve the resulting system, the associated matrix is calculated and than inverted using a python script. With this calculation we know V_+, V_- and i and so R_{out}. We indicated with the superscript (or subscript) $i = 1, ..., n$, with $i = n$ being the bottom stage, the parameters belonging to the i-th stage; for instance b_1^i, is the left barrier b-parameter for the i-th stage and b_2^i the same for the right barrier. The calculation is carried out for the "standard" stage configuration discussed in section 2.4.5, i.e. we only consider the two complementary configurations $b_1^i = 0$ and $b_2^i = 1$, or, $b_1^i = 1$ and $b_2^i = 0$. We call the first case configuration zero, indicated with $c_i = 0$, and the second case configuration one, indicated with $c_i = 1$. Each configuration of the bisector can be indicated by the binary string $c_1, ..., c_n$, which corresponds to the binary representation of $(k - 1)$, see section 2.4.5. Plots in the rest of the section are plotted as a function of the "Configuration" of the bisector, indicated by the fractional value $f = k/2^n$. We list for clarity's sake some values of f for different n and k:

- $n = 1 \quad 2^n = 2 \quad k = 1, 2 \quad f = 0.5, 1$
- $n = 2 \quad 2^n = 4 \quad k = 1, 2, 3, 4 \quad f = 0.25, 0.5, 0.75, 1$
- ...

The results for a $n = 1$, $n = 2$, $n = 3$ stages Bisector are reported in Fig.89.

An interesting behaviour emerges, in particular we see by inspection that there is a simple relationship between R_{out} values for bisectors of different n. Every new bisection stage introduces new intermediate fractions, or configuration. We see by inspection that R_{out} for the new intermediate R_{out} can be derived from the previous R_{out} values according to:

$$R_{out}((f_1 + f_2)/2) = \frac{R_{out}(f_1) + R_{out}(f_2)}{2} + h(n). \tag{6.2}$$

The value h is a general resistance increase that only depends on n and is indicated by the arrows in Fig. 89. To better visualize the behaviour of h, we can plot h vs different configurations for different bisector stages. From Fig. 90, we see that h indeed only depends on n. We now show that it is possible to find an expression for $h(n)$ and to do this we plot $\delta h = h(n + 1) - h(n)$. From the numerical calculation in Fig. 91, we see that $\delta h(n)$ follows an exponential law;

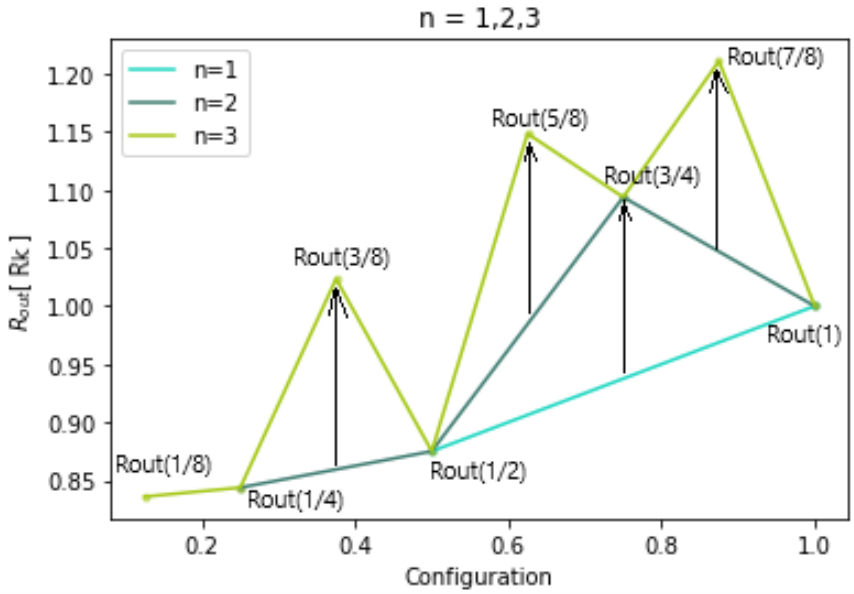

Figure 89: R_{out} for different n and different later barrier configuration. On the configuration axis we have $\frac{k}{2^n}$.

we convert the values of $\delta h(n)$ into a fraction using an ad hoc Python library (fractions) since the script outputs decimal numbers and we find they are equal to negative powers of 2. We now plot the same Fig. 91, but in log_2 scale. It is found from Fig. 92 that $log_2(\delta h(n))$ is rather precisely described by the relation:

$$log_2(\delta h(n)) = -2n - 3;$$

this means that $h(n)$ has the following property (in units of R_K):

$$h(1) = constant \tag{6.3}$$

$$h(n+1) - h(n) = \frac{1}{2^{2n+3}}. \tag{6.4}$$

Plugging $n = 0$ in Eq. 6.4, we speculate that $h(1) = 1/8$, so we can write:

$$h(n) = \frac{1}{8} \sum_{i=0}^{n-1} 2^{-2i}. \tag{6.5}$$

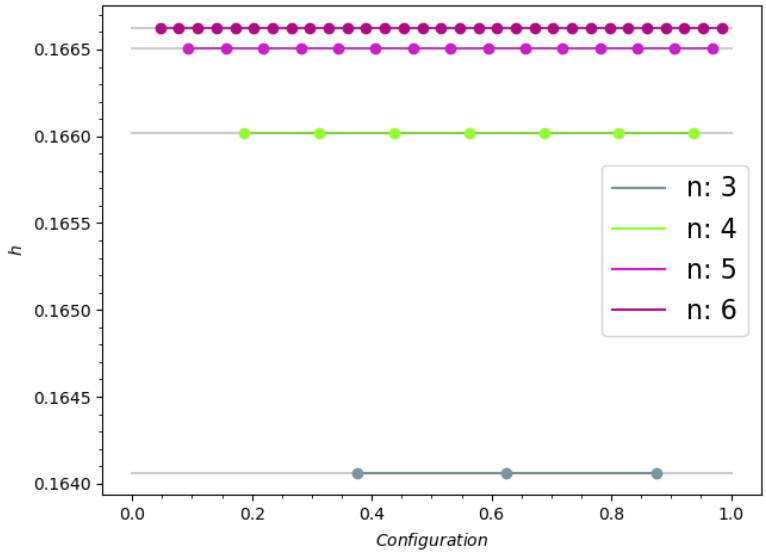

Figure 90: h for different n and different barrier configurations (in units of R_K). On the configuration axis we have $\frac{k}{2^n}$,

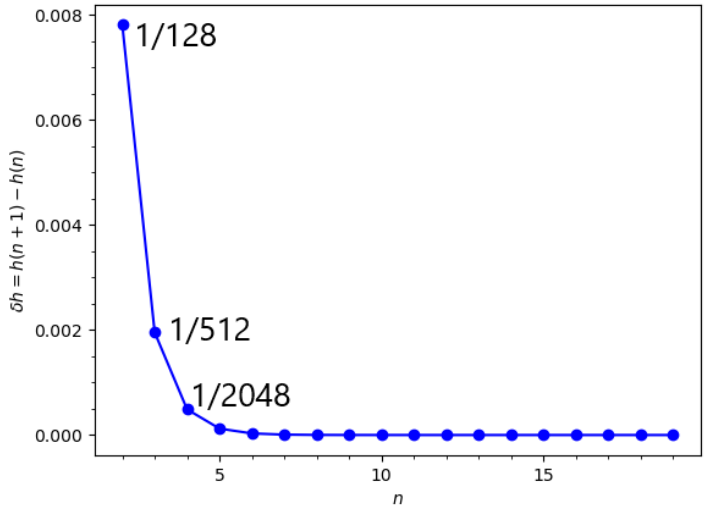

Figure 91: Numerical δh for different n (in units of R_K).

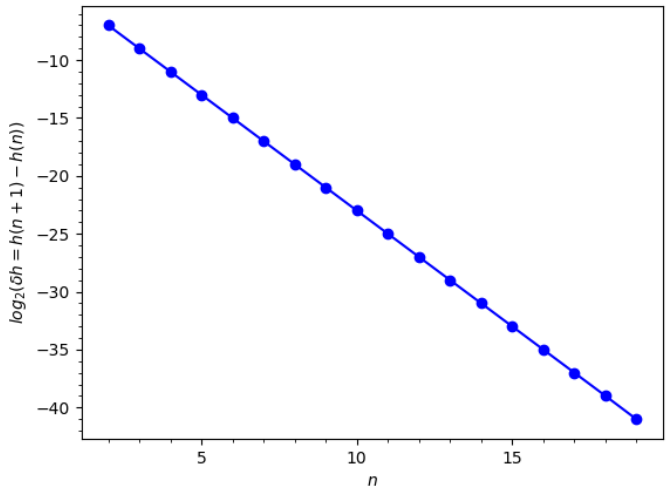

Figure 92: Numerical $log_2(\delta h)$ for different n (in units of R_K).

Which can also be written in a closed form as

$$h(n) = \frac{2^{2n} - 1}{3 \times 2^{2n+1}}. \tag{6.6}$$

From Fig. 93, we see that this formula predicts very precisely the $h(n)$ values obtained by the numerical code.

Interestingly, the empirical rule we found seems to indicate the emergence of a fractal function $R_{out}(f)$, as visible in Fig. 94, reporting R_{out} for a larger number n of stages.

6.2 Analytical model

Given the surprisingly simple recursive behaviour of R_{out}, we implemented an analytical model to explain the numerical results.

We begin by reminding for any Hall bar like in Fig. 95, we have a Hall voltage:

$$V_T - V_B = IR_0, \tag{6.7}$$

where $R_0 = R_K/2$ because two edge channels are used. So in general for every QH circuit branch working at $\nu = 2$, we have $V_B = V_T - I_{branch}R_0$, where I_{branch} is the total current flowing in the portion of the Hall bar under consideration.

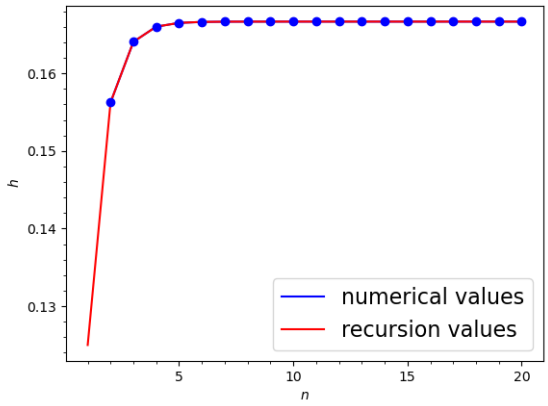

Figure 93: Comparison between the numerical value of $h(n)$ and the one derived from the empirical rule at Eq. (6.6).

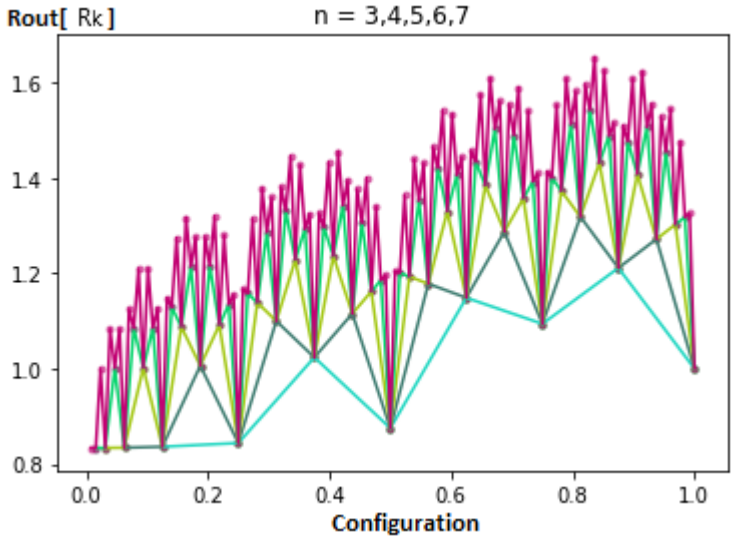

Figure 94: Other values of R_{out} for larger n values (in units of R_K).

Since we will take V_B as a reference we call $\tilde{V} = V_B$.

We now add one barrier separating two branches and we work out the voltage drops across the barrier, using the previous notation. From Fig. 96, we see that the voltage drop along both upper and lower edges of the Hall bar is $R_0 I$, i.e. the same of a resistance R_0 traversed by a current I. This means that we can model

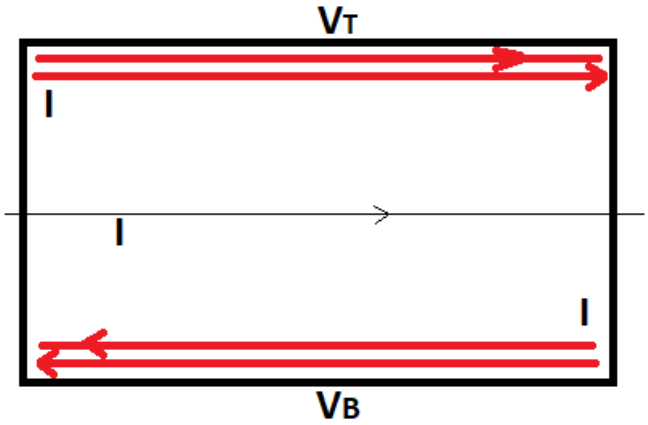

Figure 95: Hall bar with a total flowing current I, that we indicate with a thin grey line.

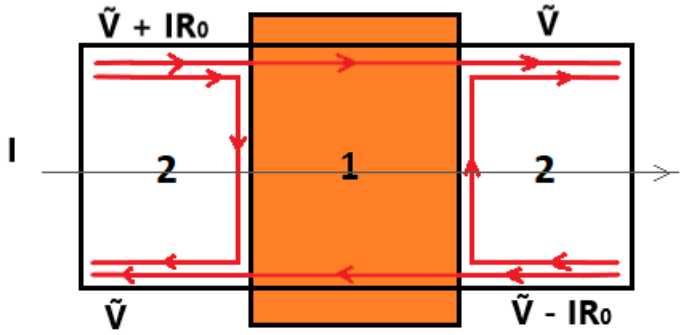

Figure 96: QH circuit branch with one barrier.

voltage drops across a single barrier and on the same edge, with a resistance R_0 traversed by the current flowing in the QH circuit branch.

The same argument can be extended to multiple barriers in series on multiple parallel branches and Fig. 97 shows an application of this model on a specific QH circuit. From Fig. 98 we see that the injection of current through contacts introduces a further voltage drop IR_0 that can be modelled as an additional R_0 resistance in series with the current source; this comes from the quantum Hall voltage drop for $\nu = 2$. From Fig. 98, this model indicates, which is the correct result for this QH circuit. Differently $V_+ - V_- = (5/3)IR_0$, if we remove the additional R_0 resistance in the resistive network and we compute the voltage

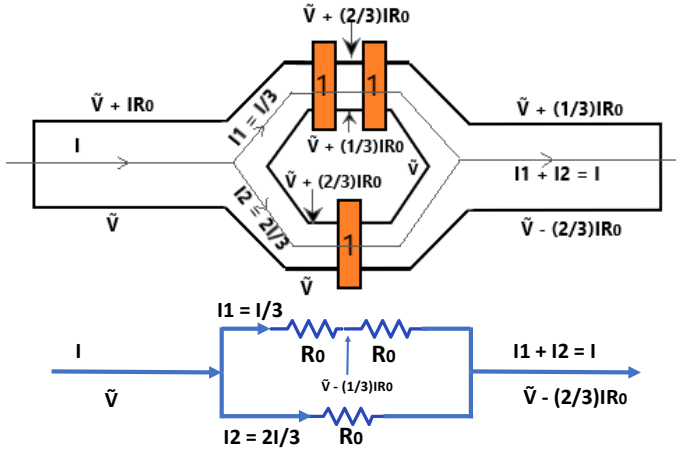

Figure 97: QH circuit resistive model.

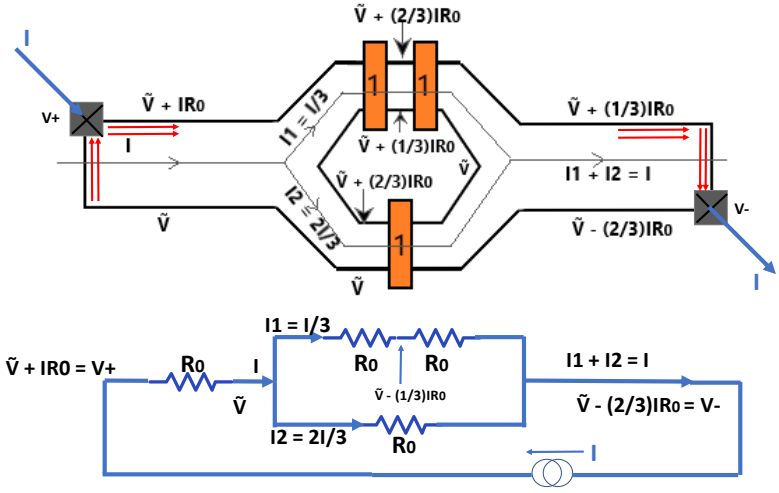

Figure 98: QH circuit resistive model with measurement contacts.

drop at the two extreme ends we find $(2/3)IR_0 \neq V_+ - V_-$ and so the model would not work.

6.2.1 Calculation of R_{out}

Now, the whole Bisector device can be seen under the light of this resistive picture, in fact each of its configurations can be brought in the form of Fig.96

i.e. with vertical barriers (Fig. 99).

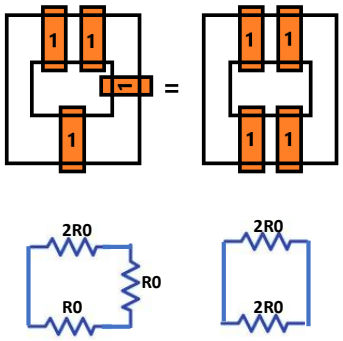

Figure 99: n=1 Bisector barrier shift for configuration 0.

Now we can find a general formula for $Rout(c_1...c_i...c_n)$, where $c_1...c_i...c_n$ is the binary string corresponding to the binary representation of the integer k in the formula $f = k/2^n$. The task is accomplished by mapping the n-stage bisector to a resistance network (Fig. 100). We notice that, once we choose a

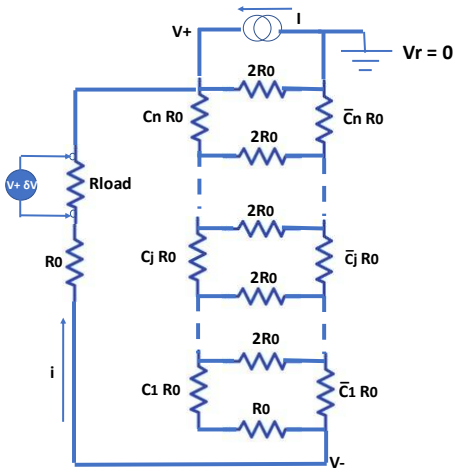

Figure 100: Generic Bisector mapped on the resistive network. The effect of measurement contacts and non-ideal measurement is included. $\bar{c_j}$ is the complement of the c_j configuration.

configuration, each stage of the resistance network can be turned into a star of resistances via the Δ-Y transformation [40].

From now on we enumerate each stage of the configuration from bottom to top using the index j ($j = 1$ is the bottom stage), and so here we will use j as a subscript or superscript to numerate each stage parameter.

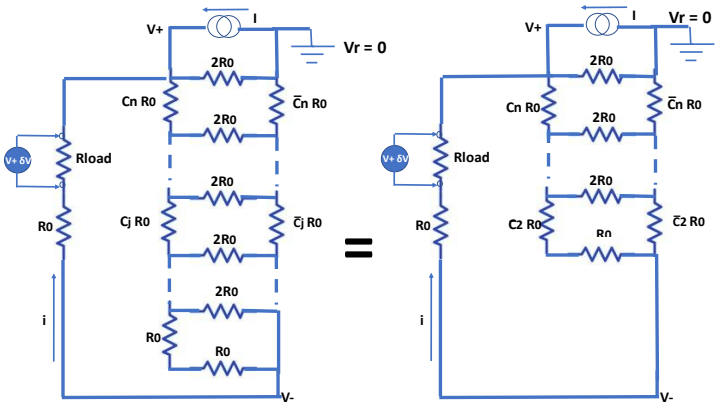

Figure 101: Equivalence between a n stages bisector with the last stage in configuration one and a n-1 stages bisector.

One simplification occurs when stage j = 1 is in configuration one ($c_1 = 1$), in fact the whole stage reduces to one resistance R_0; thus we have explained why $R_{out}(c_1...c_i...c_{n-1}1) = R_{out}(c_1...c_i...c_{n-1})$ (Fig. 101).

So if we Δ-Y transform all the stages bottom to top the simplified circuit looks like Fig. 102. The quantities in Fig. 102, R_R, R_L and R_B, are found from the following recursive scheme, where all resistances are written in units of R_0.

$$R_B^1 = 1/4 \quad R_L^1 = 1/2 \quad R_R^1 = 1/2 \tag{6.8}$$

$$R_B^j = R_B^{j-1} + \frac{(R_R^{j-1} + \bar{c}_j)(R_L^{j-1} + c_j)}{R_R^{j-1} + R_L^{j-1} + 3} \tag{6.9}$$

$$R_R^j = \frac{2(R_R^{j-1} + \bar{c}_j)}{R_R^{j-1} + R_L^{j-1} + 3} \tag{6.10}$$

$$R_L^j = \frac{2(R_L^{j-1} + c_j)}{R_R^{j-1} + R_L^{j-1} + 3} \tag{6.11}$$

In these recursive relations, it can be noted that $R_L^j + R_R^j = 1$ for any i (in fact $R_{out}(11...1) = R_{out}(1) = 1 + R_L^1 + R_R^1 = 2$). So Eq.s 6.9, 6.10 and 6.11 can

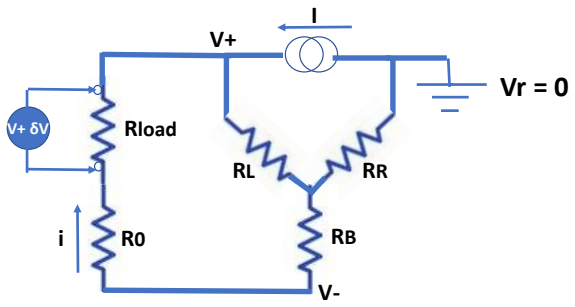

Figure 102: Trasformed resistive Bisector.

be simplified as follows:

$$R_B^1 = 1/4 \quad R_L^1 = 1/2 \quad R_R^1 = 1/2 \tag{6.12}$$

$$R_B^j = R_B^{j-1} + R_L^j R_R^j \tag{6.13}$$

$$R_R^j = \frac{(R_R^{j-1} + \bar{c}_j)}{2} \tag{6.14}$$

$$R_L^j = \frac{(R_L^{j-1} + c_j)}{2}. \tag{6.15}$$

From Eq.s 6.14, 6.15 and 6.16 we can compute a closed form for $R_B^n(c_n..c_j..c_1)$, $R_R^n(c_n..c_j..c_1)$ and $R_L^n(c_n..c_j..c_1)$ by substituting the expression $(j-1)$-th into the successive j-th one. The calculation is rather tedious and it is left to Appendix B.

From the circuit in Fig. 102, one easily can find δV and i, and so R_{out}. This last quantity is also the output resistance of the n-stage Bisector for a generic configuration and that is:

$$R_{out}^n(c_n...c_j...c_1) = 1 + R_L^n(c_n...c_j...c_1) + R_B^n(c_n...c_j...c_1). \tag{6.16}$$

If $c_n...c_j...c_1$ ends with a string of N ones, you can consider the equivalent case of an $n - N$ stages Bisector.

Now, having found the expression for R_{out} for a generic Bisector configuration, we can also find the parameter $h(n)$. To do this, we invert Eq. 6.2 and plug in the R_{out} results for the f_1, f_2 fractions and for the intermediate one $(f_1 + f_2)/2$. And we indeed find that $h(n)$ is configuration-independent and that

$$h(n) = \frac{2^{2n} - 1}{3 \times 2^{2n}}.$$

Or, using units of $R_K = 2R_0$;

$$h(n) = \frac{2^{2n} - 1}{3 \times 2^{2n+1}}. \tag{6.17}$$

The explicit calculation is reported in Appendix B.

The limitations of this resistive model are that it only allows to calculate the voltage drop across current injecting terminals, and these must lie on the same edge. For example this model does not allow to calculate the quantities measured by Fang et al. in [11] (Fig. 17) and for this reason it should not be considered a resistive equivalent of the QH circuit.

This calculation is useful because in this manner the perturbed values of the fractions of R_K, caused by non-ideal measurements, can be precisely corrected and so the precision of a bisection QH circuit can be assessed isolating problems due to R_{out} from other (maybe) less quantifiable precision loss effects. As we saw from the numerical calculation plots, R_{out} is dependent on the bisector configuration, so we might reach a point where the approximation $R_{load} \to \infty$ (ideal measurement) or equivalently the condition $R_{load} \gg R_{out}$ is no longer valid. It must also be said that, even if R_{out} grows with n, it remains limited.

7

Conclusions

We now summarize the main results of this thesis.

We study a novel quantum Hall circuit that uses an edge bisection scheme to obtain a custom fractional value of R_K. The edge bisection works with field-effect barriers (mixers or gates) on a GaAs/AlGaAs two dimensional electron gas (2DEG). During the thesis, Hall bar devices integrating these barriers have been fabricated and characterized at filling factors $\nu = 2$ and $\nu = 4$. The fractional values of R_K obtainable via the bisection scheme have been assessed.

A key element to determine the precision of the studied QH bisection circuit is the maximum current or voltage bias that the Hall bar can handle before a QH breakdown. To study this effect it was important to check if we obtained the correct behaviour from the gates. We obtained the correct number of fractional values for R_K and for this reason, the QH breakdown of the bar has been explored by biasing a single mixer with different voltage values. It was found that the device works safely at all filling factor configurations for voltage bias values $< 10\,\mathrm{mV}$ and breakdown currents of the order of $1\,\mu\mathrm{A}$. It is interesting to stress that the architecture studied in this thesis was found to be more susceptible to break down with respect to ungated structures. Even if this QH breakdown current value appears to be low compared to bias currents used in top precision metrology that do not have gating features, it can still be useful for calibration applications.

Unfortunately, the ultimate precision of the bisection mechanism could not be determined, presumably due to a parallel conduction of the sample, as revealed by SdH oscillations that do not display a dissipation-less regime ($\rho_{xx} = 0$) despite the cryogenic temperatures ($T = 300\,\mathrm{mK}$) achieved with a ^{3}He cryostat.

In addition, the influence of a finite output resistance on the QH circuit has been studied, both with a numerical and an analytical approach. In the last case, a resistive model of the QH circuit has been developed and discussed. The general result obtained was an open question in Ref. [5]. From these studies we found a general formula for R_{out} and shown that despite a growth as a function of n, R_{out} remains limited even in the $n \to \infty$ limit. The resistive analytical model turns out (with some caveats) to be a very useful tool that allows to simplify the calculation of voltage drops for this kind of bisection circuit, by mapping them on a simple resistive network.

7.1 Perspectives

One open question is whether it is actually possible to achieve metrological precision with the discussed device architecture and whether this scheme can also be extended to novel 2D materials such as graphene. In fact, graphene could be particularly interesting material for metrology [41] due to the unique Landau energy spacing of graphene $\Delta E_{LL} \propto \sqrt{B}$ [42], which implies that the energy spacing between the lowest Landau level and the first excited one is substantially higher than GaAs at standard magnetic fields of few Teslas and allows surviving the QHE up to room temperatures [42].

Besides various portings of conventional 2DEG QH metrology approaches into a graphene platform such as simple graphene Hall bars [43] or graphene QHARS [44], other approaches based on Corbino disks (a hollow disk) with regions of p-dopend and n-doped graphene [45] [46] in which edge currents flow in opposite directions, thus cancelling each other in certain regions of the disk and yielding a R_K fraction depending on the wiring, have been proposed [47]. In this fashion a bisection scheme based on n or p regions on the same graphene sheet could be in principle reproduced.

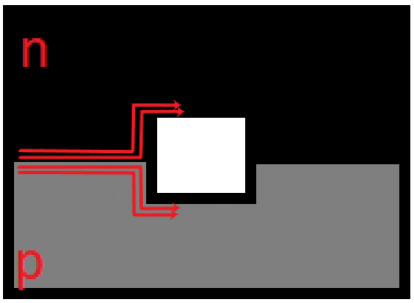

Figure 103: Simple graphene bisection.

A simple bisection circuit that is not externally controllable can be made from a graphene sheet with a hole punched in the middle. The sheet top part is n-doped and the bottom one is p-doped. The edge channels which emerges from these filling factors is shown in Fig. 103 with $\nu = 2$ (for electrons) and $\nu = -2$ (for holes). The practical realization of these devices is challenging, since one would need to realize metal contacts on the n-p interfaces. Furthermore the edges traveling at a n-p interface might not properly equilibrate to lead to a vanishing longitudinal voltage drop. Still, given the less stringent requirements of graphene in terms of temperature and magnetic field, the exploration of this class of devices is surely a perspective which is worth to investigate.

A Effect of the insert filters

The original cryostat insert is filtered via two π filters in series, then two low pass filters and again, on the output line, two low pass RC filters in series and two π filters. Fig. 104 shows the two type of filters used. The π filters only filter

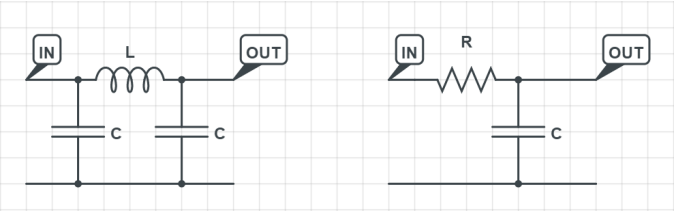

Figure 104: Insert filters. The one on the left is a π filter, the one on the right is a low pass RC filter. $R = 1\,\mathrm{k\Omega}$ and $C = 47\,\mathrm{nF}$.

frequencies above 10 MHz and are not relevant in this discussion, so we neglect them and will concentrate only on the double low pass filters.

In this section we discuss what happens on the measurements, if the filters are not removed. In fact the first measurements were taken with a filtered insert. It turned out this was not a good idea, so the next measurements were taken with an unfiltered insert. These are the one shown in the Experimental Results chapter, while here we only show some measurements taken with filters and using the (R, ϕ) representation.

As usual, we passed 1 V through a bias resistance of $10\,\mathrm{M\Omega}$ that is much larger than the resistance of the Hall bar, so we expect to measure 100 nA at all probed terminals. All gate contacts have been put to ground. The output current measured at contact 2 was 83.40 nA and the signal had a fase of 153.28 deg. Getting further away from contact 1 and 16 one measures progressively less current and a different phase (e.g. 61.65 nA 111.49 deg, at contact 11). Injecting current through 1 and measuring at 16 we strangely found 86.10 nA, because the two lines are bonded on the same contact and so it is a short. The sample was removed and a metal bridge was put, connecting the contact 1 and 16 on the sample holder, correctly measuring 100 nA. So we came to the conclusion that the insert filters were affected by the larger Hall bar resistance and were modifying the measurement. In fact, lowering the lock-in frequency from 17.206 Hz to 13.206 Hz the low current value measured at 16 grew to 89.47 nA.

First of all let us compute the cut-off frequency at $-3\,\mathrm{dB}$ of one line of the insert circuit without considering the Hall bar device. The result is shown in Fig. 105. We find a cut-off of 455 Hz, that is far from the frequencies used for

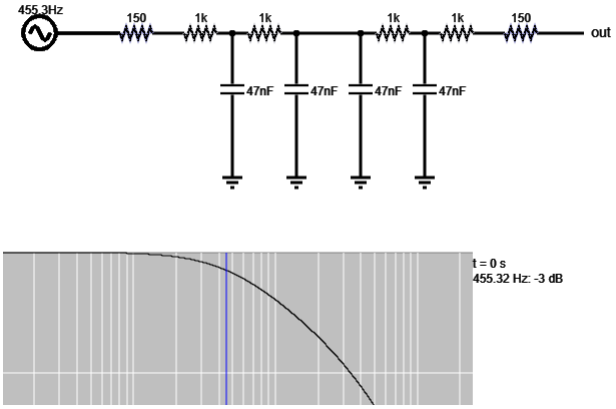

Figure 105: Simulation of the insert circuit [48] without the Hall bar, the cut-off frequency at -3dB is around 455 Hz. In the range $13 - 14$ Hz the gain is of the order of -0.01 dB. 150 Ω is the cable resistance.

our AC measurements (in the range of $13 - 14$ Hz, Fig. 105).

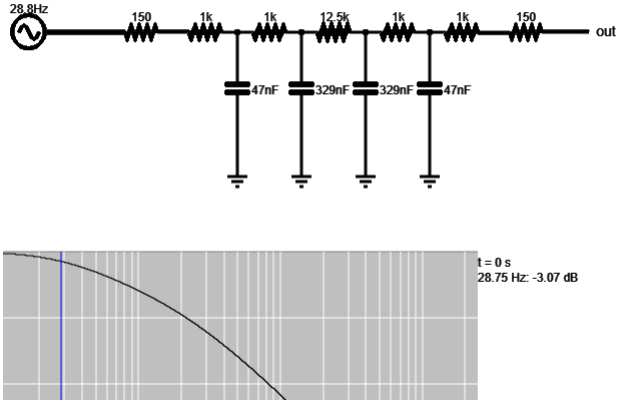

Figure 106: Simulation [48] of the insert circuit with a Hall bar at $\nu = 2$ (12.5 kΩ), the cut-off frequency at -3 dB is around 28 Hz. In the range $13-14$ Hz the gain is of the order of -1 dB 108.

The situation changes if we add the contribution of the Hall bar to the line resistance. Considering that we use 7 Ohmic contacts, whose lines are filtered with a double low pass and which are all floating during the measurement, the

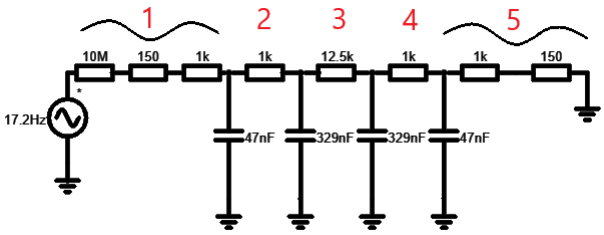

Figure 107: Simple model of the insert circuit with the Hall bar and its lines [49].

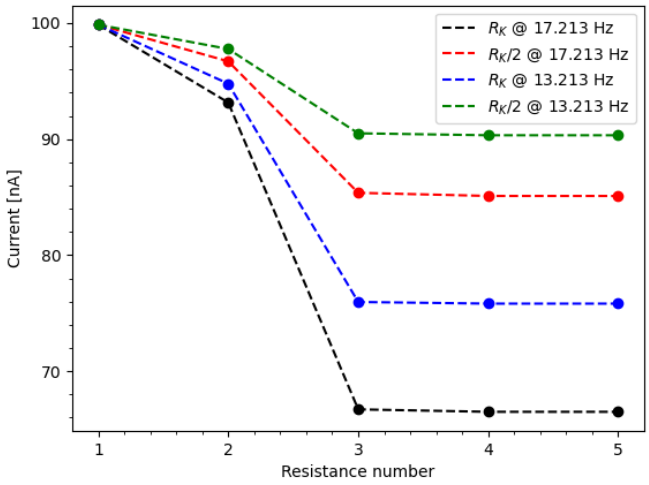

Figure 108: Current loss from left to right (1: first circuit branch to 5: last circuit branch) along the line in Fig. 107.

Hall bar input has (grossly approximating) seven 47 nF capacitors in parallel. The same holds for the output, too. Fig. 106 and Fig. 107 shows how that the input and the output capacitance of the Hall bar resistance change according to the approximation made. In this case, the cutoff frequency is dramatically lowered and part of the current injected at the beginning of the line is lost on the grounded capacitors along the line as reported in Fig. 108.

Since each contact line is capacitively grounded, some current is lost along the edge of the sample, and this causes V_{xx} to be different from zero for integer filling factors because a finite voltage drop along the edge develops as the current leaks. The magnitude of the shift of the V_{xx} curves also depends on the chirality:

for example Fig. 109 for anticlockwise chirality, the effect of current loss in more visible at the first two contacts the current arrives (before being completely drained). The effect for clockwise chirality is reported in Fig. 110.

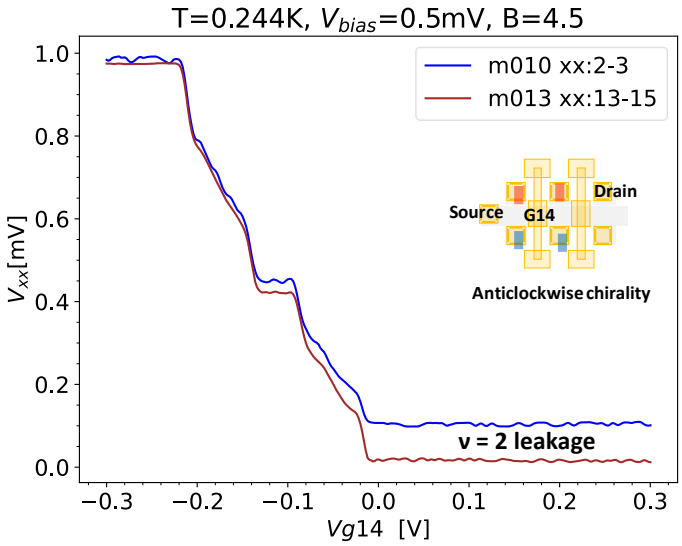

Figure 109: $V_{xx} \neq 0$ at $\nu = 2$ effect is apparent before the channel reaches the OUT drain (bottom contacts). Anticlockwise chirality.

The diagonal voltages across the gate in Fig. 111 is also affected by the current loss. So in this case deviations in the plateau values are caused both by $R_{xx} \neq 0$ due to the suggested parallel conduction and by current leakage through the filters. The deviations appear more prominent than without filters.

In Fig. 112, the capacitive nature of the circuit can be seen by the 2D phase plot of V_d vs V_{g12} and V_{g14}, where a signal with a phase of 90 degrees is present.

The low value of cutoff frequency is confirmed by the plot in Fig. 113 that shows a diagonal voltage drop that flattens to zero once we hit the cutoff frequency.

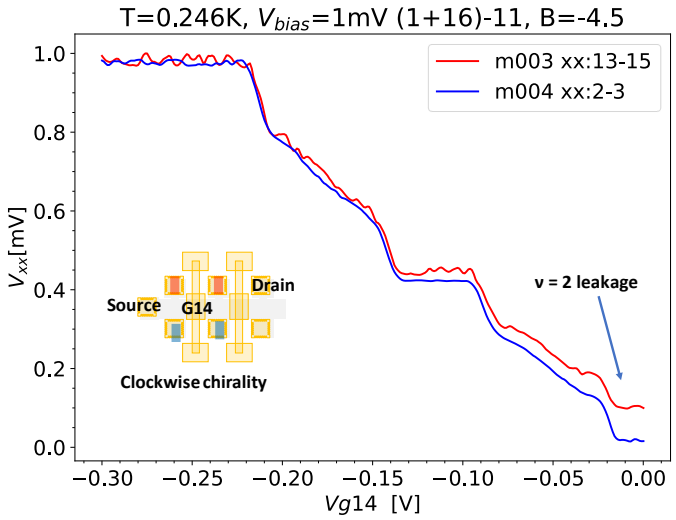

Figure 110: $V_{xx} \neq 0$ at $\nu = 2$ effect is apparent before the channel reaches the OUT drain (top contacts). Clockwise chirality.

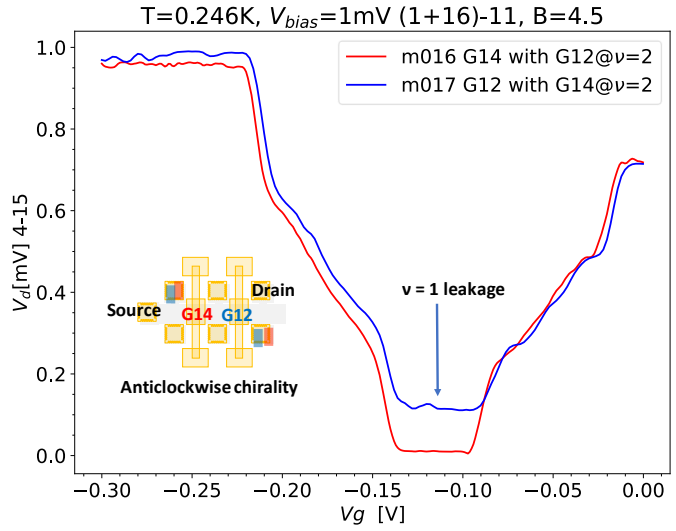

Figure 111: $V_d \neq 0$ at $\nu = 1$ effect.

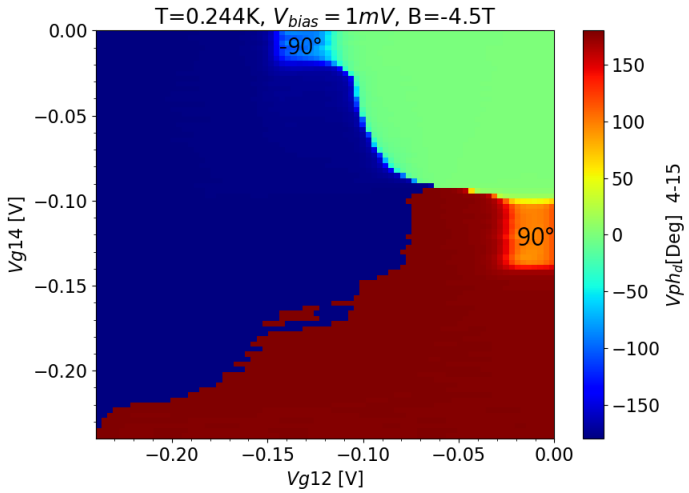

Figure 112: V_d phase 2D map. Contacts wiring is the same as Fig. 111.

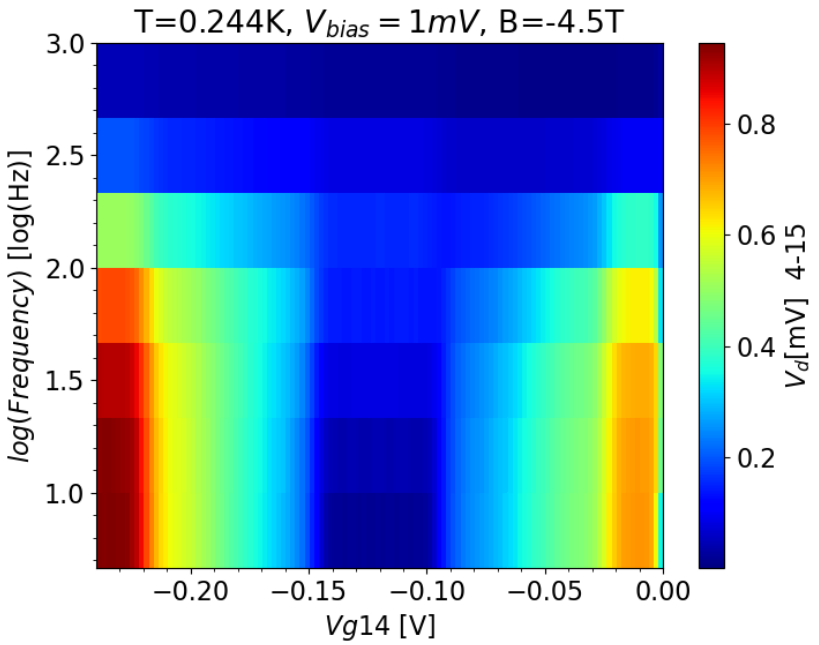

Figure 113: Value of V_d (diagonal as Fig. 111) vs bias frequency and gate 14 voltage bias. Increasing the bias frequency, V_d curve flattens to zero as we hit the cutoff frequency.

B Other R_{out} details

B.1 Non-standard values

The script has been written in such a way that it is possible to calculate R_{out} also for non-standard configurations (i.e. $b_1^i = 0$ and $b_2^i = 0$ or $b_1^i = 1$ and $b_2^i = 1$) for a total of 2^{2n} configurations but a distinctive pattern has not been found (Fig.114).

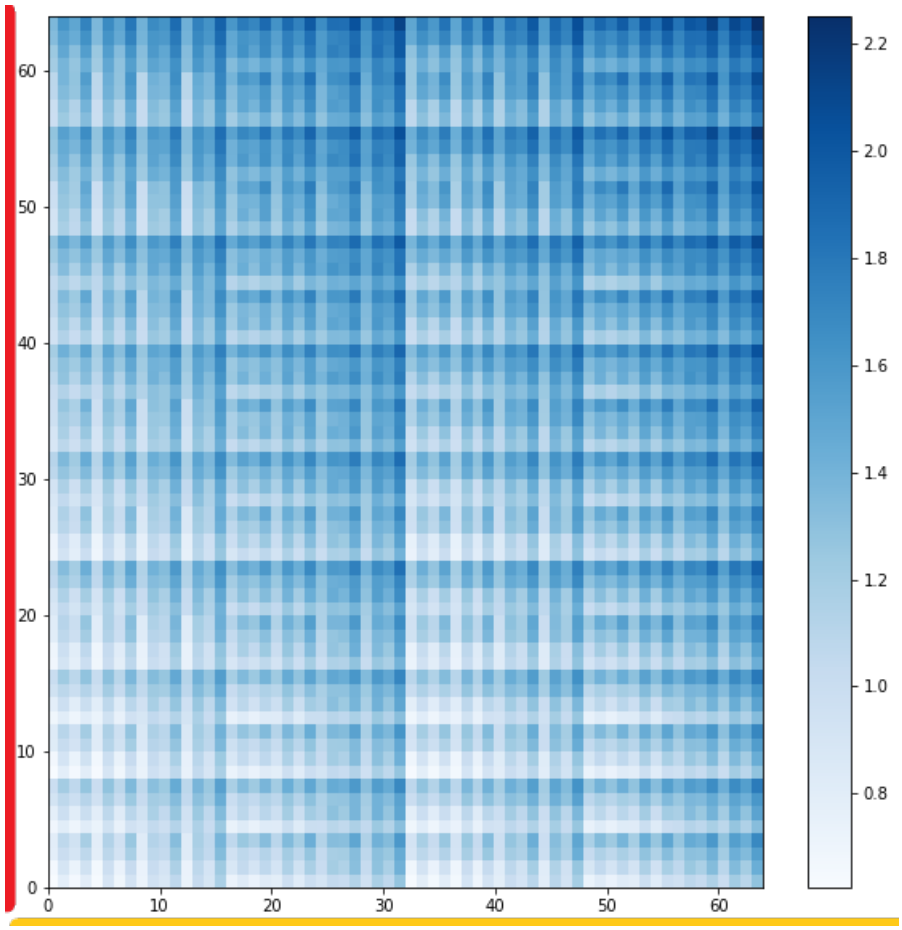

Figure 114: Standard and non-standard values of R_{out} for a $n = 6$ stages Bisector. Red axis is the decimal representation of $b_1^1...b_1^i...b_1^n$, yellow axis of $b_2^1...b_2^i...b_2^n$. The color bar is in units of R_K.

B.2 Calculation

Eq. 6.2 can be rewritten using the binary strings of configuration that correspond to the fractions in the R_out argument.

$$h(n) = R^n_{out}(c_n...c_j...0) - \frac{R^n_{out}(c_n...c_j...1) + R^n_{out}(c_n...c_j...0-1)}{2}, \tag{B.1}$$

where $c_n...c_j...0$ is a configuration string with $c_1 = 0$, $c_n...c_j...1$ is a configuration string with $c_1 = 1$ and $c_n...c_j...0-1$ is the result of the binary subtraction of $c_n...c_j...0$ with 1.

Now we find the closed form for the R_R, R_L and R_B.

$$R^2_R = \frac{\frac{1}{2} + \bar{c_2}}{2} \tag{B.2}$$

$$R^3_R = \frac{\frac{\frac{1}{2}+\bar{c_2}}{2} + \bar{c_3}}{2} \tag{B.3}$$

$$R^4_R = \frac{\frac{\frac{\frac{1}{2}+\bar{c_2}}{2}+\bar{c_3}}{2} + \bar{c_4}}{2} \qquad = \frac{1}{2^4}(1 + 2\bar{c_2} + 2^2\bar{c_3} + 2^3\bar{c_4}) \tag{B.4}$$

$$\vdots$$

$$R^n_R(c_n...c_1) = \frac{1}{2^n}\sum_{j=1}^{n}(2^{j-1}\bar{c_j}) \tag{B.5}$$

The last equality is true if we force $\bar{c_1} = 1$. In a similar manner if we force $c_1 = 1$:

$$R^n_L(c_n...c_1) = \frac{1}{2^n}(\sum_{j=1}^{n} 2^{j-1}c_j). \tag{B.6}$$

From Eq. (6.12):

$$R_B^2 = \frac{1}{4} + \frac{1}{2^2}\sum_1^2 2^{j-1}c_j - \frac{1}{2^4}(\sum_1^2 2^{j-1}c_j)^2 \tag{B.7}$$

$$R_B^3 = \frac{1}{4} + \frac{1}{2^3}\sum_1^3 2^{j-1}c_j - \frac{1}{2^6}(\sum_1^3 2^{j-1}c_j)^2 + \frac{1}{2^2}\sum_1^2 2^{j-1}c_j - \frac{1}{2^4}(\sum_1^2 2^{j-1}c_j)^2 \tag{B.8}$$

$$\vdots$$

$$R_B^n(c_n...c_1) = \sum_{j=1}^n \frac{1}{2^j}(\sum_{l=1}^j 2^{l-1}c_l) - \sum_{j=1}^n \frac{1}{2^{2j}}(\sum_{l=1}^j 2^{l-1}c_l)^2. \tag{B.9}$$

We define the sums in brackets in (B.8) as k_j, or the decimal representation of the first js configurations minus the fact that c_1 is forced to 1. Same goes for the brackets in (B.5), that we call k.

Using $R_{out}^n(c_n...c_1) = 1 + R_L^n(c_n...c_1) + R_B^n(c_n...c_1)$, we substitute each term in the definition of $h(n)$:

$$h(n) = R_{out}^n(c_n...0) - \frac{R_{out}^n(c_n...1) + R_{out}^n(c_n...0-1)}{2}. \tag{B.10}$$

The configuration $c_n...0+1$ is equivalent to $c_n...1$. The terms k and k_j for configuration $c_n...0+1$ must be replaced with $k+1$ and k_j+1, while for configuration $c_n...0-1$ with $k-1$ and k_j-1. We get:

$$h(n) = 1 + \sum_{j=1}^n \frac{1}{2^j}(k_j) - \sum_{j=1}^n \frac{1}{2^{2j}}(k_j)^2 + \frac{1}{2^n}(k)$$

$$-\frac{1}{2}(2 + \sum_{j=1}^n \frac{1}{2^j}(k_j-1) - \sum_{j=1}^n \frac{1}{2^{2j}}(k_j-1)^2 + \frac{1}{2^n}(k-1)$$

$$+\sum_{j=1}^n \frac{1}{2^j}(k_j+1) - \sum_{j=1}^n \frac{1}{2^{2j}}(k_j+1)^2 + \frac{1}{2^n}(k+1)).$$

Simplifying everything (in units of R_0):

$$h(n) = \sum_{j=1}^n 2^{-2j} = \frac{1}{3} - \frac{4^{-n}}{3} = \frac{2^{2n}-1}{3*2^{2n}}$$

So in units of $R_K = 2R_0$:

$$h(n) = \frac{2^{2n} - 1}{3 * 2^{2n+1}}. \tag{B.11}$$

For all zeros configuration we have:

$$R_{out}(\underbrace{0...0}_{n}) = 1 + \frac{1}{2^n} + \sum_{j=1}^{n}(\frac{1}{2^j} - \frac{1}{2^{2j}}) = \frac{5 + 4^{-n}}{3} R_0 \tag{B.12}$$

Bibliography

[1] K. v. Klitzing; G. Dorda; M. Pepper, "New method for high-accuracy determination of the fine-structure constant based on quantized hall resistance", Phys. Rev. Lett. **45**, 494 (1980).

[2] B. Jeckelmann and B. Jeanneret, "The quantum hall effect as an electrical resistance standard", Rep. Prog. Phys. **64**, 1603 (2001).

[3] B. Scherer Hansjörg; Camarota, "Quantum metrology triangle experiments: a status review", Measurement Science and Technology **23**, 124010 (2012).

[4] D. A. Syphers, F. F. Fang, and P. J. Stiles, "Multiple connected quantized resistance regions", Surface Science **142**, 208 (1984).

[5] Z. S. Momtaz, S. Heun, G. Biasiol, and S. Roddaro, "Cascaded quantum hall bisection and applications to quantum metrology", Phys. Rev. Applied **14**, 024059 (2020).

[6] G. Grosso and G. Pastori Parravicini, *Solid state physics, second edition* (Elsevier, Academic Press, 2014).

[7] F. J. Ahlers, B. Jeanneret, F. Overney, J. Schurr, and B. M. Wood, "Compendium for precise ac measurements of the quantum hall resistance", Metrologia **46**, R1 (2009).

[8] Y. Zhong, J. J. Li, Q. Zhong, Y. F. Lu, J. T. Zhao, and X. S. Wang, "GaAs/AlGaAs quantum hall resistance devices with AuGeNi and in contacts", in 2012 conference on precision electromagnetic measurements (2012), pp. 386–387.

[9] M. Ortolano and L. Callegaro, "Circuit models and spice macro-models for quantum hall effect devices", Measurement Science and Technology **26**, 085018 (2015).

[10] M. Marzano, T. Oe, M. Ortolano, L. Callegaro, and N.-H. Kaneko, "Error modelling of quantum hall array resistance standards", Metrologia **55** (2018).

[11] F. Fang and P. Stiles, "Quantized magnetoresistance in multiply connected perimeters in two-dimensional systems", Physical Review 8 **29**, 10.1103/PhysRevB.29.3749 (1984).

[12] M. Büttiker, "Absence of backscattering in the quantum hall effect in multiprobe conductors", Physical Review B **38**, 9375 (1988).

[13] A. O. Slobodeniuk, I. P. Levkivskyi, and E. V. Sukhorukov, "Equilibration of quantum hall edge states by an ohmic contact", Physical Review B **88**, 165307 (2013).

[14] N. Paradiso, S. Heun, S. Roddaro, D. Venturelli, F. Taddei, V. Giovannetti, R. Fazio, G. Biasiol, L. Sorba, and F. Beltram, "Equilibration of integer quantum hall edge channels studied by scanning gate microscopy", in (2010).

[15] Microposit, *S1813 photoresist datasheet*, https://amolf.nl/wp-content/uploads/2016/09/datasheets_S1800.pdf.

[16] K. W. Goossen, J. E. Cunningham, T. H. Chiu, D. A. B. Miller, and D. S. Chemla, "Non-alloyed Al ohmic contact to GaAs for GaAs/Si interconnect compatibility", in International technical digest on electron devices meeting (1989), pp. 409–410.

[17] A. M. Burke, D. E. J. Waddington, D. J. Carrad, R. W. Lyttleton, H. H. Tan, P. J. Reece, O. Klochan, A. R. Hamilton, A. Rai, D. Reuter, A. D. Wieck, and A. P. Micolich, "Origin of gate hysteresis in p-type si-doped AlGaAs/GaAs heterostructures", Phys. Rev. B **86**, 165309 (2012).

[18] A. El Hdiy and S. Mouetsi, "Identification of traps in an epitaxied AlGaAs/GaAs/AlGaAs quantum well structure", Journal of Applied Physics **108**, 034513 (2010).

[19] M. Grayson and F. Fischer, "Measuring carrier density in parallel conduction layers of quantum hall systems", Journal of Applied Physics **98**, 10.1063/1.1948529 (2005).

[20] L. Cui, Y. Zeng, Y. Zhang, W. Zhou, L. Shang, T. Lin, and J. Chu, "Beating patterns in the shubnikov-de haas oscillations originated from spin splitting in $In_{0.52}Al_{0.48}As/In_{0.65}Ga_{0.35}As$ heterostructures: experiment and calculation", Elsevier, Physica E **83**, 114 (2016).

[21] I. A. Yugova, A. Greilich, D. R. Yakovlev, A. A. Kiselev, M. Bayer, V. V. Petrov, Y. K. Dolgikh, D. Reuter, and A. D. Wieck, "Universal behavior of the electron g factor in $GaAs/Al_xGa_{1-x}As$ quantum wells", Phys. Rev. B **75**, 245302 (2007).

[22] A. V. Shchepetilnikov, Y. A. Nefyodov, I. V. Kukushkin, and W. Dietsche3, "Electron g-factor in GaAs/AlGaAs quantum wells of different width and barrier al concentrations", Phys.: Conf. Ser. **456**, 10.1088/1742-6596/456/1/012035 (2013).

[23] J. Mejía-Salazar, N. Porras Montenegro, and L. E. Oliveira, "Quantum confinement and magnetic-field effects on the electron g factor in $GaAs-(Ga, Al)$ as cylindrical quantum dots", Journal of physics. Condensed matter : an Institute of Physics journal **21**, 455302 (2009).

[24] T. Ito, W. Shichi, S. Morisada, M. Ichida, H. Gotoh, H. Kamada, and H. Ando, "Quantum confinement effects on electron spin g-factor in semiconductor quantum well structures", physica status solidi c **3**, 3496 (2006).

[25] T. Englert, D. Tsui, A. Gossard, and C. Uihlein, "g-factor enhancement in the 2d electron gas in GaAs/AlGaAs heterojunctions", Surface Science **113**, 295 (1982).

[26] S. Studenikin, M. Korkusinski, M. Takahashi, J. Ducatel, A. Padawer-Blatt, A. Bogan, D. G. Austing, L. Gaudreau, P. Zawadzki, A. Sachrajda, Y. Hirayama, L. Tracy, J. Reno, and T. Hargett, "Electrically tunable effective g-factor of a single hole in a lateral GaAs/AlGaAs quantum dot", Communications Physics **2**, 159 (2019).

[27] M. T. Björk, A. Fuhrer, A. E. Hansen, M. W. Larsson, L. E. Fröberg, and L. Samuelson, "Tunable effective g factor in InAs nanowire quantum dots", Phys. Rev. B **72**, 201307 (2005).

[28] A. C. H. Rowe, J. Nehls, R. A. Stradling, and R. S. Ferguson, "Origin of beat patterns in the quantum magnetoresistance of gated InAs/GaSb and InAs/AlSb quantum wells", Phys. Rev. B **63**, 201307 (2001).

[29] M. E. Raikh and T. V. Shahbazyan, "Magnetointersubband oscillations of conductivity in a two-dimensional electronic system", Phys. Rev. B **49**, 5531 (1994).

[30] T. H. Sander, S. N. Holmes, J. J. Harris, D. K. Maude, and J. C. Portal, "Determination of the phase of magneto-intersubband scattering oscillations in heterojunctions and quantum wells", Phys. Rev. B **58**, 13856 (1998).

[31] K. Panos, R. R. Gerhardts, J. Weis, and K. v. Klitzing, "Current distribution and hall potential landscape towards breakdown of the quantum hall effect: a scanning force microscopy investigation", New Journal of Physics **16**, 113071 (2014).

[32] K. Shizuya, "Current distribution in hall bars and breakdown of the quantum hall effect", Physica E: Low-dimensional Systems and Nanostructures **6**, 148 (2000).

[33] M. E. Cage, "Current distributions in quantum hall effect devices", Journal of research of the National Institute of Standards and Technology **102**, 677 (1997).

[34] G. Nachtwei, "Breakdown of the quantum hall effect", Physica E: Low-dimensional Systems and Nanostructures **4**, 79 (1999).

[35] P. Haremski, M. Mausser, A. Gauß, K. von Klitzing, and J. Weis, "Electrically induced breakdown of the quantum hall effect at different hall bar widths: visualizing the edge- and bulk-dominated regimes within a quantum hall plateau", Physical Review B **102**, 205306 (2020).

[36] K. Shizuya, "Field-induced breakdown of the quantum hall effect", Physical Review B **60**, 8218 (1999).

[37] S. Kawaji, K. Hirakawa, M. Nagata, T. Okamoto, T. Fukuse, and T. Gotoh, "Breakdown of the quantum hall effect in GaAs/AlGaAs heterostructures due to current", Journal of the Physical Society of Japan **63**, 2303 (1994).

[38] G. Nachtwei, G. Lütjering, D. Weiss, Z. H. Liu, K. von Klitzing, and C. T. Foxon, "Breakdown of the quantum hall effect in periodic and aperiodic antidot arrays", Phys. Rev. B **55**, 6731 (1997).

[39] T. Sanuki, S. Takaoka, K. Oto, K. Murase, and K. Gamo, "Breakdown of quantum hall effect in two dimensional electron system with antidot arrays", Solid-State Electronics **42**, 1165 (1998).

[40] M. Raugi, *Lezioni di elettrotecnica* (Pisa University Press, 2013).

[41] F. Poirier Wilfrid; Schopfer, "Can graphene set new standards?", Nature Nanotechnology **5**, 171 (2010).

[42] D. M. Pakdehi, *Optimization of epitaxial graphene growth for quantum metrology* (PhD thesis at Physikalisch-Technische Bundesanstalt, 2020).

[43] M. Kruskopf, D. K. Patel, C.-I. Liu, A. F. Rigosi, R. E. Elmquist, Y. Wang, S. Bauer, Y. Yin, K. Pierz, E. Pesel, M. Götz, and J. Schurr, "Graphene quantum hall effect devices for ac and dc resistance metrology", in 2020 conference on precision electromagnetic measurements (cpem) (2020), pp. 1–2.

[44] A. R. Panna, I.-F. Hu, M. Kruskopf, D. K. Patel, D. G. Jarrett, C.-I. Liu, S. U. Payagala, D. Saha, A. F. Rigosi, D. B. Newell, C.-T. Liang, and R. E. Elmquist, "Graphene quantum hall effect parallel resistance arrays", Phys. Rev. B **103**, 075408 (2021).

[45] S. Matsuo, S. Takeshita, T. Tanaka, S. Nakaharai, K. Tsukagoshi, T. Moriyama, T. Ono, and K. Kobayashi, "Edge mixing dynamics in graphene p–n junctions in the quantum hall regime", Nature Communications **6**, 8066 (2015).

[46] B. Özyilmaz, P. Jarillo-Herrero, D. Efetov, D. A. Abanin, L. S. Levitov, and P. Kim, "Electronic transport and quantum hall effect in bipolar graphene $p-n-p$ junctions", Phys. Rev. Lett. **99**, 166804 (2007).

[47] C.-I. Liu, D. K. Patel, M. Marzano, M. Kruskopf, H. M. Hill, and A. F. Rigosi, "Quantum hall resistance dartboards using graphene $p-n$ junction devices with corbino geometries", AIP Advances **10**, 035205 (2020).

[48] P. Falstad, *Filters simulator applet*, `https://www.falstad.com/afilter/`.

[49] P. Falstad, *Analog circuit simulator applet*, `https://www.falstad.com/circuit/`.

[50] D. Yoshioka, *The quantum hall effect* (Springer, 2002).

[51] S. M. Girvin, "The quantum hall effect: novel excitations and broken symmetries", Topological Aspects of Low Dimensional Systems, ed. A. Comtet, T. Jolicoeur, S. Ouvry, F. David (Springer-Verlag, Berlin and Les Editions de Physique, Les Ulis), `arXiv:cond-mat/9907002` (2000).

[52] A. MacDonald, "Introduction to the physics of the quantum hall regime", arxiv.org, `arXiv:cond-mat/9410047` (1994).

Ringraziamenti

Vorrei ringraziare i miei relatori per la loro pazienza ed estrema disponibilità. Ringrazio il Prof. Stefano Roddaro che, non solo ha sempre trovato il tempo di chiarire prontamente ed efficientemente ogni mio dubbio, mi ha anche spinto a valorizzare i più piccoli dettagli. Ringrazio il Dr. Stefan Heun per la fondamentale assistenza in laboratorio e per avermi guidato con la sua grandissima esperienza da sperimentatore. Anche lui sempre disponibile a chiarire ogni minimo dubbio, nonostante i mille impegni. Ringrazio nuovamente entrambi per la loro umanità, specie durante il periodo di pandemia, in particolare il Prof. Roddaro per essere stato disposto ad ascoltare anche qualche mia stravagante idea e il Dr. Heun per la sua pazienza nel rispondere e leggere le mie email di protesta durante il periodo di chiusura del laboratorio.

Infine, ringrazio genericamente tutti quelli che mi hanno accompagnato in questa esperienza.